# ROTORDYNAMIC CHARACTERISTICS OF THE HPOTP (HIGH PRESSURE OXYGEN TURBOPUMP) OF THE SSME (SPACE SHUTTLE MAIN ENGINE)

Prepared for: George C. Marshall Space Flight Center

under

Contract NAS8-34505

By

Dara W. Childs, Ph.D., P.E.

Seal RD-1-84
30 January 1984





Turbomachinery Laboratories
Mechanical Engineering Department

# ROTORDYNAMIC CHARACTERISTICS OF THE HPOTP (HIGH PRESSURE OXYGEN TURBOPUMP) OF THE SSME (SPACE SHUTTLE MAIN ENGINE)

prepared for
George C. Marshall Space
Flight Center
Alabama 35812
under
CONTRACT NAS8-34505

Principal Investigator
Dara W. Childs

Turbomachinery Laboratories
Mechanical Engineering Dept.
Texas A&M University
College Station, Texas 77843

Turbomachineries Laboratories Report
RD-1-84, 30 January 1984

ROTORDYNAMIC CHARACTERISTICS OF THE HPOTP
(HIGH PRESSURE OXYGEN TURBOPUMP) OF THE
SSME (SPACE SHUTTLE MAIN ENGINE)

ABSTRACT

Problems associated with subsynchronous motion at approximately 450 Hz for FPL turbopumps is the subject of this study. The basic model for the HPOTP is discussed including the structural dynamic model for the rotor and housing, component models for the liquid and gas seals, turbine-clearance excitation forces, and impeller-diffuser forces. Linear and nonlinear analyses are carried out to meet the following objectives:

(b) Provide an explanation for the observed subsynchronous motion via nonlinear simulation results.

(c) Evaluate proposed hardware changes in the HPOTP to remedy current difficulties.

The analysis results support the following conclusions:

(a) The current HPOTP is marginally stable and is subject to excessive synchronous bearing loads due to its proximity to the second critical speed.

(b) Observed subsynchronous motion can be simulated by transient models which include bearing-clearance nonlinearities. These nonlinearities generate forced subharmonic response at observed frequencies for the models considered. Bearing clearances and very light damping are sufficient to develop subsynchronous motion in an otherwise (zero-bearing-clearance) stable model.

(c) Replacing the boost-impeller labyrinth seals with "damper" seals without stiffening the rotor reduces synchronous bearing loads, and improves stability, but it does not necessarily eliminate subsynchronous motion.

(d) By linear analysis, replacing the current main impeller with a shrouded-

inducer impeller eliminates both synchronous and subsynchronous problems associated with the second critical speed.

(e) Replacing the current rotor with a stiffened rotor without changing seals eliminates subsynchronous motion but does not necessarily reduce synchronous bearing loads.

(f) Replacing the current rotor with a stiffened rotor and replacing the current boost impeller labyrinth seals with damper seals sharply reduces synchronous bearing loads, increases rotor stability, and eliminates subsynchronous motion.

LIST OF FIGURES

page

LIST OF TABLES

# I. INTRODUCTION

A discussion of the rotordynamic characteristics of the HPOTP is expedited by a review of figures 1, 2, and 3 which illustrate, respectively, the SSME powerhead and turbopump arrangement, the rotating assembly, and two of the zero-running-speed, coupled, rotor-housing modes for the current (unstiffened-rotor) turbopump. The two modes of figure 3 involve relatively small motion of the housing with large rotor motion corresponding to the first and second bending modes of the rotor. The 179 Hz mode is dominated by the overhung-turbine displacement, while the maximum displacement of the 530 Hz mode is at the main impeller, with relatively small motion at the turbines. The modes of figure 3 are calculated for the bearing stiffnesses $K_{bi}$ = 500,000 lbs/in. The calculated linear critical speeds for the turbopump including gyroscopic coupling, seal forces, impeller forces, etc. are at approximately 12,500 cpm (208 Hz) and 32,500 cpm (540 Hz).

Initial rotordynamics problems with the HPOTP involved subsynchronous motion at approximately 200 Hz associated with the first critical speed. This problem was eliminated by changing the turbine interstage seal from a stepped-labyrinth configuration to a constant-clearance, honeycomb-stator seal. The turbopump still displays subsynchronous motion in the 250 Hz frequency range at start up, and subsynchronous motion associated with the first critical speed continues to be of concern at higher power levels.

The second problem associated with the HPOTP involves subsynchronous vibrations at approximately 400-420 Hz. This motion tended to initiate when the running speed reached the appropriate excitation frequency, and persisted as subsynchronous motion when the running speed was increased. A failure and explosion of the HPOTP occurred in a test run when the running speed first

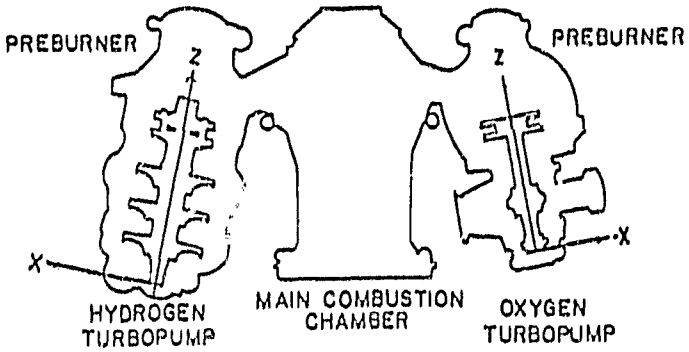


Figure 1. SSME powerhead component arrangement and local rotor coordinate systems.

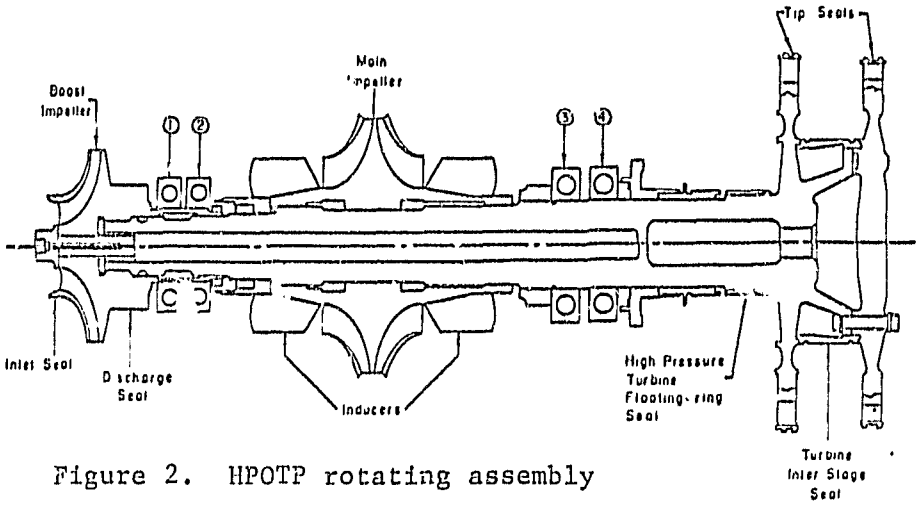


Figure 2. HPOTP rotating assembly

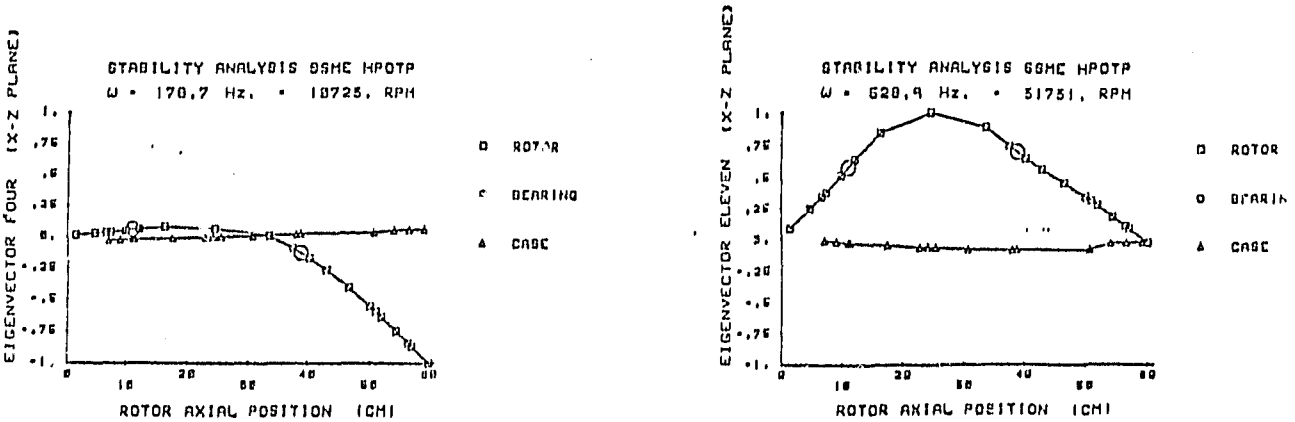


Figure 3. Undamped, zero-running-speed, nominal-rotor/housing modes associated with the first and second critical speed.

traversed the maximum-amplitude frequency range and then was reduced to and remained at the now synchronous frequency. The failure was attributed to an inadequate bearing-carrier design which caused unequal load sharing of the bearings. Subsequently, redesigned bearing carriers eliminated the "400 Hz" subsynchronous motion. The general feeling was that the new bearing carrier designs caused a more equal load sharing and maintained the correct axial bearing preloads, thus realizing the "expected" radial stiffness of the bearings and elevating the rotor second critical speed.

The bearing-carrier redesign was sufficient to yield a reliable pump for RPL operations; however, demonstration of FPL capability has been impeded by repeated occurrence of subsynchronous motion in the 450-500 Hz frequency range. The incidence of this motion rarely occurs during initial operation at higher power levels, but tends to develop after an accumulation of time and develops more rapidly with higher synchronous vibration levels. However, once a unit begins to "whirl", it will repeatedly whirl, generally with progressively increasing severity. The frequency of the subsynchronous motion is sometimes at a fixed fraction of running speed ranging from 88 to 95%. This "tracking" characteristic is in marked contrast to the earlier "400 Hz" phenomenon where the whirl-frequency of the subsynchronous motion remained constant, relatively independent of running speed.

Post-run inspection of turbopumps has revealed that, although the balls in some bearings, primarily bearing 2, appear to be unblemished, their diameters have in fact, been reduced by as much as 0.17 mm in some cases. The cause of this dimensional attrition is unknown, but has been ascribed to either excessive radial loads or the absence of radial loads which leads to skidding.

At various times, the following hypotheses have been put forward to explain the observed "450 Hz" subsynchronous motion:

(a) Motion associated with the second-critical-speed modeshape of figure 2 is marginally stable, with the destabilizing forces provided by impeller-diffuser interaction forces [1]. The principal deficiency of the linear-stability-analysis approach is the predicted whirl frequency of 530 Hz versus observed whirl frequencies around 450 Hz; hence, a linear model with nominal bearing coefficients predicts "supersynchronous" motion instead of subsynchronous motion. The bearing stiffness coefficients of linear models must be reduced substantially below current estimates to yield subsynchronous motion at the correct whirl frequency.

(b) The subsynchronous motion arises from bearing-stiffness asymmetry which rotates at the cage precessional speed and yields an additional forced excitation at approximately 90% of running speed. This is the only hypotheses which explains the "tracking" observed in the data and was put forward by Bernie Rowan at Rocketdyne before his untimely death. The problem with this explanation is that, according to Rocketdyne, backward-whirling motion would be excited, and the backwards modes are predicted to be heavily damped. The phenomenon of bearing-stiffness asymmetry exciting subsynchronous motion had been investigated by Yamamoto [2], who demonstrated experimentally that insertion of a single large ball into a ball bearing could yield stable, forced-subsynchronous motion.

(c) The subsynchronous motion is a nonlinear phenomenon arising from motion in and out of the bearing dead-band* clearances. To the

---

*Clearances provided between the outer case of the bearing and the housing to allow axial slipping.

author's knowledge, Steve Winder at MSFC first suggested this mechanism following the "400 Hz" HPOTP explosion. Simulations by the author [1] show that the bearing dead-bands can lower the peak vibration amplitudes into the operating range, as predicted by Yamamoto [3]. However, no demonstration has been made that the bearing clearances yield a lower whirl frequency than predicted by linear analysis.

The present report documents the results of (a) linear analysis to characterize the nominal model and (b) nonlinear transient simulations which support the hypotheses that bearing dead-band clearances are principally responsible for the observed subsynchronous motion. No analyses were carried out to examine Rowan's hypothesis of rotating assymetry.

While the causes of subsynchronous motion remain uncertain, the following hardware modifications are being undertaken and considered:

(a) The rotating assembly is being stiffened in the vicinity of bearings 1 and 2.

(b) The current labyrinth designs for the boost-impeller wear-ring seals are being replaced with damper seals which use a roughened stator and a smooth rotor. A swirl brake to reduce the inlet tangential velocity is also being implemented for the inlet seal.

(c) Replacement of the current unshrouded inducers with shrouded inducers has been suggested, with the seals at the outer surface of the inducer developing relatively large stiffness and damping.

The consequences of these changes on the rotordynamic characteristics of the HPOTP are examined in this study.

Continuing uncertainties exist as to the correctness of models for the individual force elements of the rotordynamic model. The author carried out a systematic examination of the literature concerning "best" component models

at the start of this study [4], and the preceding Phase B report [5] utilized the best available models and best available current estimates for parameters of these models. The current report provides a review of the changes and advances which have been made in component models of seal forces and again presents parameters for a "best-available" rotordynamic model.

In summary, the results reported in this study were carried out to meet the following objectives:

(a) develop the best-available model for the HPOTP in terms of forces developed by seals, impellers, turbines, etc.,

(b) examine the linear dynamic characteristics of the HPOTP in terms of stability and synchronous-response predictions,

(c) evaluate and develop explanations for the observed "450 Hz" sub-synchronous motion, and

(d) evaluate the prospects of proposed hardware modifications for improving the dynamic characteristics of the HPOTP.

The following chapter briefly describes the structure and components of the rotordynamic model, with succeeding sections describing the results of linear and nonlinear analyses.

## II. THE ROTORDYNAMICS MODEL

### Introduction

This section briefly reviews the elements of the HPOTP rotordynamic models used in this study. Some of the actual "numbers" used to define the model are provided in Appendix A.

### Structural Dynamics Model

The structural dynamics model of the rotor and the housing form the basic framework of the turbopump model. Both the housing and rotor structural dynamics models used here were developed by Rocketdyne. A general three-dimensional finite-element approach was used to model the HPOTP housing without the rotor. A lumped parameter model was developed for the rotor using beam structural elements and lumped masses and inertias. The rotor-dynamics model uses modes from the housing model (without the rotor) and free-free rotor modes. The current (unstiffened) rotor model was developed by Bernie Rowan several years ago. The stiffened-rotor model was provided in 1983 by Robert Beatty.

### Bearings

The bearings are the structural elements which tie the rotors and housings together. As illustrated in figure 2, there are two sets of bearings. The net load from each set is transmitted through a plate-cylinder structure to the housing. The bearings in a bearing set are axially preloaded against each other, but are not designed to accept axial thrust loads from the turbo-pumps. A balance-piston arrangement at the discharge of the main impeller absorbs axial thrust, and radial clearances are provided at the bearing outer races to allow the bearings to slip axially without developing excessive axial loads.

Experience and limited test data [6] for the SSME bearings indicate a nominal stiffness of approximately .5 X $10^6$ lbs/in which is approximately one half of the values predicted by A. B. Jones-based analysis [7]. This nominal value was used throughout the current study. Prior analyses [5] examined the influence of feasible changes in the bearing stiffnesses and show the expected results, viz., the first and second critical speeds move up and down as the bearing stiffnesses are increased or decreased.

The bearings are in series with the intermediate structure which transmits their load to the housing. The values used for those local stiffnesses are

$$K_{s1} = K_{s2} = 2 \times 10^6 \text{ lbs/in}$$
$$K_{s3} = K_{s4} = 4 \times 10^6 \text{ lbs/in} \qquad (1)$$

The radial clearances provided at the bearings to permit axial motion provide an essential "dead-band" nonlinearity. The clearance values used throughout most of this study are

$$\delta_P = \delta_T = .5 \times 10^{-3} \text{ in} \qquad (2)$$

where P and T denote pump and turbine bearings.

Liquid Seals

Liquid wear-ring seals are provided at the inlet and discharge of the boost impeller. The current inlet seal is a stepped labyrinth design with four cavities. The current discharge seal is a three segment, stepped seal. Each constant-radius seal segment has a series of circumferential grooves.

Experience and limited test data [8] have shown that labyrinth or serrated seals of the type currently employed on the impeller inlet and discharge yield stiffness and damping coefficients which are substantially smaller than corresponding values for smooth constant clearance seals. Replacing the current grooved boost-impeller wear-ring seals with plain annular seals has the potential

for a beneficial increase in stiffness and damping in the HPOTP. In fact, as the following discussion explains, various additional possibilities exist for optimizing seals.

The force-motion model for liquid seals has the form

$$-\begin{Bmatrix} F_X \\ F_Y \end{Bmatrix} = \begin{bmatrix} K & k \\ -k & K \end{bmatrix} \begin{Bmatrix} X \\ Y \end{Bmatrix} + \begin{bmatrix} C & c \\ -c & C \end{bmatrix} \begin{Bmatrix} \dot{X} \\ \dot{Y} \end{Bmatrix} + \begin{bmatrix} M & m \\ -m & M \end{bmatrix} \begin{Bmatrix} \ddot{X} \\ \ddot{Y} \end{Bmatrix} \qquad (5)$$

In this model (X,Y) are the components of the relative motion between the rotor and housing. Black, et al. [9, 10] were responsible for most of the analytical developments related to the analysis of seals leading to the definition of stiffness, damping, and added-mass coefficients. His analysis demonstrates that the "cross-coupled" stiffness coefficient, k, arises solely due to fluid rotation within the seal. As a fluid element proceeds axially along an annular seal, shear forces at the rotor accelerate or decelerate the fluid tangentially until an asymptotic value is reached. For a seal with the same directionally-homogeneous surface-roughness treatment on the rotor and the housing, the average asymptotic tangential velocity is $R\omega/2$ where R is the seal radius and $\omega$ is the rotor running speed.

The cross-coupled stiffness coefficient k acts in opposition to the direct damping coefficient C to destabilize rotors. Hence, steps which can be taken to reduce the net fluid rotation within a seal will improve rotor stability by reducing k. The modifications which have been undertaken for the boost-pump impeller seals propose to increase net damping by the following physical mechanisms:

(a) The analysis of von Pragenau [11] has recently predicted that the asymptotic tangential velocity can be modified if a different surface roughness is used for the rotor and stator elements. Rough rotor/smooth stator and smooth rotor/rough stator combinations yield

higher and lower asymptotic values, respectively. Von Pragenau calls the rough-stator/smooth-rotor configuration a "damper seal" because of its enhanced stability characteristics. The roughness has the additional potential benefit of reducing leakage. Damper seal configurations are presently under consideration for both the inlet and discharge seals of the boost impeller. Analysis by Childs and Kim [12] based on a finite-length solution [13] yield predictions which are consistent with von Pragenau. Rocketdyne develops the desired roughness on both boost-impeller seals by a knurled indentation pattern on the stator.

(b) If the inlet tangential velocity can be reduced, the high axial velocities in a cryogenic seal are such that the fluid may proceed through a seal without substantially increasing its tangential velocity. An anti-vortex web has been introduced at the inlet to the boost-impeller inlet seal to reduce the inlet tangential velocity and yield a reduced k. This practice has been followed previously for the labyrinth seals of high pressure compressors [14].

Tests of an annular seals in which the stator has the knurled roughness pattern used by Rocketdyne and a smooth rotor have recently been carried out at TAMU. The results, which are documented in [15], show good agreement between theory [12] and experiment with respect to k and C, but a serious underprediction of K and M. For the present study, calculated values are used for k, C, m, and M, but calculated values for K are corrected upwards based on the results of [15]. For calculation, inlet tangential velocity for the discharge seal is assumed to be asymptotic, i.e., $R\omega/2$. However, the swirl web at the inlet seal is assumed to be effective in reducing this value by a factor of two. Seal coefficients used in the rotordynamic calculations

are provided in Appendix A.

Gas Seals

The HPOTP turbines are shrouded, and single-cavity tip seals are provided to reduce leakage between the turbine shroud and the stator. The interstage seal between the turbines uses a honeycomb stator element with a smooth rotor and inlet anti-vortex ribs to reduce the inlet tangential velocity component. A floating-ring shaft seal is provided at the turbine discharge to restrict leakage of the hot turbine gases towards the lox within the pump. The flow across this seal is choked.

Rotordynamic coefficients for the tip seals use Rocketdyne calculations. Nelson's [16] method is used for the turbine interstage seal and the high-pressure turbine seal. His analyses apply to constant-clearance or convergent taper geometries, account for the development of tangential velocity within the seals, and different but directionally-homogeneous surface roughness on the rotor and stator.

A constant-clearance configuration was originally used for the turbine interstage seal. More recently, Rocketdyne has replaced the constant-clearance configuration with a convergent taper. Computed rotordynamic coefficients are provided in Appendix A for both configurations.

The "floating-ring" nature of the high-pressure turbine seal is such that its full reaction force can not be transmitted to the pump housing. Specifically, the seal is designed to slip before any appreciable force can be transmitted. To compensate for this situation, the calculated seal rotor-dynamic coefficients are arbitrarily reduced by a factor of 5. Calculated values are provided in Appendix A.

Turbine Clearance Excitation Forces

Clearance-excitation forces are developed by turbines due to the dependency of local efficiency on local clearances. The destabilizing force is modeled by

$$\begin{Bmatrix} F_X \\ F_Y \end{Bmatrix} = \begin{bmatrix} 0 & k_T \\ -k_T & 0 \end{bmatrix} \begin{Bmatrix} X \\ Y \end{Bmatrix} ; \quad k_T = \frac{\beta T}{D_p H} \tag{4}$$

where T is the turbine torque, $D_p$ is the average pitch diameter of the turbine blades, H is the average height, and $\beta$ defines the change in turbine efficiency due to uniform changes in clearance. Again, the components (X,Y) of Eq. (4) define the displacement of the turbine relative to the housing. Thomas initially identified this destabilizing phenomenon [17], while Alford [18] subsequently and independently developed the same model. Test results for shrouded turbines have yielded values for $\beta$ on the order of 0.6 [19]. The value of 0.4 is used in this study.

The dimensions of the HPOTP turbines are

$$D_p = 9.57 \text{ in}, \quad H = .496 \text{ in}$$

The torque and clearance-excitation coefficient ($\beta = 1$) are listed below

| | $\omega$ (cpm) | T (in -lb) X $10^4$ | $K_T$ (lb/in) |
|---|---|---|---|
| FPL | 30,960 | 6.20 | 13,060 |
| MPL | 19,841 | 2.48 | 5,230 |

Note that the $K_T$ values are for <u>both</u> turbine stages with $\beta = 1$.

Impeller-Diffuser Forces

A test program has been under way at the California Institute of Technology for some time to measure the static and dynamic forces experienced by a pump impeller in either a volute or a vaned diffuser. Chamieh et al. [10] have defined the following model on the basis of static measurements of an impeller within a vaned diffuser:

$$-\frac{1}{\rho A_2 V_2^2}\begin{Bmatrix} F_X \\ F_Y \end{Bmatrix} = \begin{bmatrix} K^* & k^* \\ -k^* & K^* \end{bmatrix} \begin{Bmatrix} X/R_2 \\ Y/R_2 \end{Bmatrix} = \begin{bmatrix} -2.0 & 0.7 \\ -0.7 & -2.0 \end{bmatrix} \begin{Bmatrix} X/R_2 \\ Y/R_2 \end{Bmatrix} \quad (5)$$

where $R_2$ is the impeller radius, $\rho$ is the fluid density, $V_2=R_2\omega$ is the impeller tip velocity, and $A_2=2\pi R_2 b_2$ is the exit flow area. Note that the direct-stiffness coefficient in Eq. (5) is negative, i.e., the impeller-diffuser force causes a reduction in rotor stiffness. From Eq. (5), the dimensional impeller-diffuser coefficients are defined by

$$\begin{aligned} \overline{K} &= K^* \frac{\rho A_2 V_2^2}{2R_2} = K^* (\pi \rho b_2 R_2^{\,2})\omega^2 \\ \overline{k} &= k^* (\pi \rho b_2 R_2^{\,2})\omega^2 \end{aligned} \quad (6)$$

More recently, Cal. Tech. researchers [21] have reported preliminary results for an extension of the model provided by Eq. (5) to include direct and cross-coupled damping terms. However, rotordynamic analysis of the HPOTP suggests that the proposed values are unrealistically high. In particular, the proposed direct damping value is large enough to eliminate any possible rotordynamic problems. The cross-coupled damping coefficient acts like a "gyroscopic-stiffening" element and also seems to be too large, since it would elevate the predicted whirl frequency to 638 Hz. In view of these uncertainties, the original simple model of Eq. (6) was used for rotor-dynamic calculations with the damping model of [21] discarded.

The dimensions of the two impellers are provided below:

Main Impeller: $R_2 = 3.35$ in, $b_2 = 1$ in

Boost Impeller: $R_2 = 2.60$ in, $b_2 = .270$ in

The following coefficients result

| | Main Impeller | | Boost Impeller | |
|---|---|---|---|---|
| | FPL | MPL | FPL | MPL |
| $\omega$ (cpm) | 30,960 | 19,841 | 30,960 | 19,841 |
| $\rho$ (Kg/m$^3$) | 1,137 | 1,137 | 1,114 | 1,114 |
| $\bar{K}$ (lb/in) | $-7.88X10^4$ | $-3.24X10^4$ | $-1.28X10^4$ | $-5,2^{\cdot}$ |
| $\bar{k}$ (lb/in) | $2.76X10^4$ | $1.13X10^4$ | 4,480 | 1,840 |

Fixed-Direction Side Loads

The hydrodynamic side loads are assumed to be proportional to speed squared. The proportionality constants are listed below

| | K (X - Z) lbs·sec$^2$ | K (Y - Z) lbs·sec$^2$ |
|---|---|---|
| Boost Impeller | $-2.806 \times 10^{-5}$ | $4.950 \times 10^{-6}$ |
| Main Impeller | $7.281 \times 10^{-5}$ | $6.117 \times 10^{-5}$ |
| Turbines | 0 | $2.379 \times 10^{-5}$ |

These coefficients yield a total main-impeller side load of 960 lbs at FPL. The side load is used in the nonlinear analysis and, by its interaction with the dead-band clearance and imbalance magnitude, has a significant influence on rotor response.

Balance-Piston Stiffness and Damping Coefficients

The balance-piston stiffness is modeled by the quadratic relationship

$$K_Z = -431.97\ \omega + .3542\ \omega^2 \qquad (7)$$

where $\omega$ is the running speed in rad/sec. However, $K_Z$ is never allowed to fall below 200,000 lbs/in. Eq. (7) fits Winder's graphical data [22]. Balance-piston damping is held at 15% of critical for all speeds. Axial motion of the rotor is only coupled to the housing in the nonlinear model. The linear model does not include this feature.

Imbalance Distribution

The imbalance distribution used in all cases consisted of the following aligned imbalances:

| | Location | Magnitude |
|---|---|---|
| (a) | Boost Impeller | .1273 gm cm |
| (b) | Main Impeller | 10.18 gm cm |
| (c) | Mid-turbine | 12.73 gm cm |

Table 1. HPOTP imbalance distribution.

While considerable uncertainty exists concerning the particular imbalance distribution in a given turbopump, the distribution of table 1 provides adequate excitation for the modes of interest.

LINEAR ANALYSIS

## Introduction

As noted above, bearing "dead-band" clearances are the significant known nonlinearity which influences rotordynamics. If the dead-band clearances are neglected, a linear model results. The present chapter concerns results of linear analysis for various models of HPOTP turbopump configurations. The following chapter concerns nonlinear-analysis results which differ in many respects from linear predictions. The linear analysis results of the present section provide an efficient and helpful characterization of the turbopump's rotordynamic characteristics.

The analysis procedure used here is basically the same as that outlined in reference [23]. Modal coordinates based on the zero-running-speed coupled rotor-housing modes are used. Gyroscopic coupling and forces due to seals, turbine clearance-excitation, the interaction of impellers and diffusers, damping, etc. couple the modal coordinates via modal stiffness, damping, and inertia matrices. The onset speed of instability for a turbopump configuration is defined by calculating the complex eigenvalues of the system dynamic matrix at various speeds. Synchronous-response amplitudes of bearing reactions and acceleration levels of accelerometers mounted on the turbopump housing due to imbalance are calculated.

Table 2 provides the distinguishing characteristics of the six turbopump configurations which are analyzed in this section. Except as otherwise noted, the six turbopump models are identical and use the nominal parameters of the preceding section and Appendix A.

Parameters of the "nominal" model were selected to represent the current flight configurations. Without additional damping, the nominal model predicts

| | Rotor | Boost-Impeller Wear-Ring Seals | Main Impeller |
|---|---|---|---|
| a. Nominal Model | current | Labyrinth | Unshrouded |
| b. Nominal Model with Damper Seals | current | Rocketdyne Damper | Unshrouded |
| c. Nominal Model with Shrouded Inducer | current | Laybrinth | Shrouded |
| d. Stiffened Rotor | stiffened | Labyrinth | Unshrouded |
| e. Stiffened Rotor with Damper Seals | stiffened | Rocketdyne Damper | Unshrouded |
| f. Stiffened Rotor with Otimized Damper Seals | stiffened | "Optimized" Damper | Unshrouded |

Table 2. Turbopump configurations for linear analysis.

an OSI (Onset Speed of Instability) at 17,200 cpm. Hence, the model was "tuned" by adding concentrated linear damping at the main impeller. This damping develops forces which are proportional to the relative velocity between the rotor and housing at this location. The linear damping coefficient, C = 5 lb sec/in, was sufficient to elevate the OSI to 30,480 cpm and is used for all models. No damping is provided at the bearings. The configurations of table 2 were selected to characterize the current flight configurations and examine the consequences of the following changes to this configuration:

(a) Replace the labyrinth, boost-impeller, wear-ring seals with damper seals.

(b) Replace the unshrouded inducer with a shrouded inducer.

(c) Stiffen the current rotor.

(d) Stiffen the current rotor and use damper seals for the boost-impeller wear-ring seals.

(e) Stiffen the current rotor and use "optimized" damper seals for the boost impeller.

Results for these configurations are provided below.

Current Flight Configuration

Figure 4 illustrates the bearing reactions for running speeds from 5,000 to 40,000 cpm. The first and second critical speeds are clearly evident, with the second critical speed having very little damping. Figure 5 (a) illustrates the same results for speeds from 5,000 cpm to FPL. Figures 5 (b) and (c) illustrate predicted acceleration levels for accelerometers mounted on the housing at the pump and turbine ends of the turbopump. Clearly, FPL is quite near the predicted second critical speed. Also, while the bearing reactions

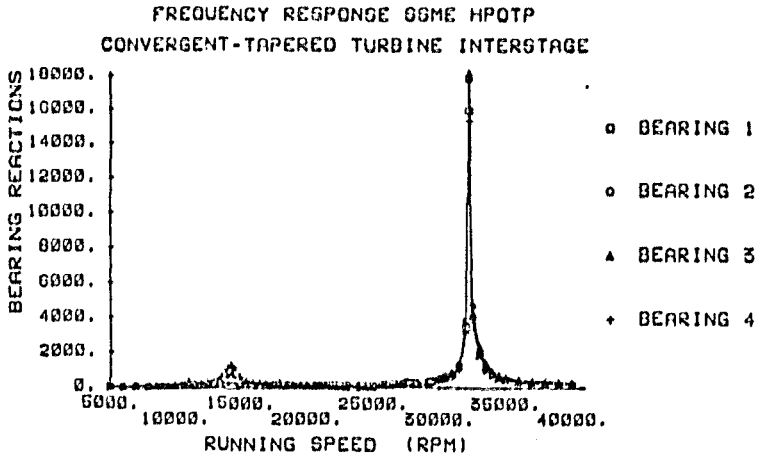


Figure 4. Bearing reactions for the nominal (current) linear model with speeds out to 40,000 cpm.

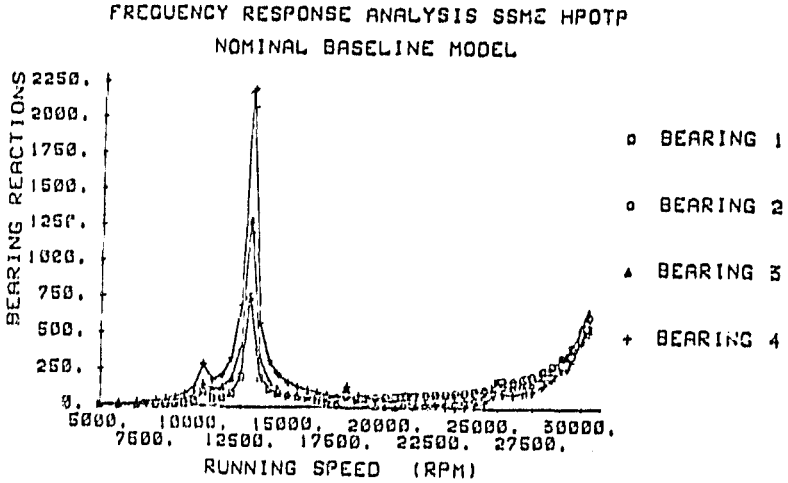


Figure 5(a). Bearing reactions for the nominal linear model with speeds out to FPL.

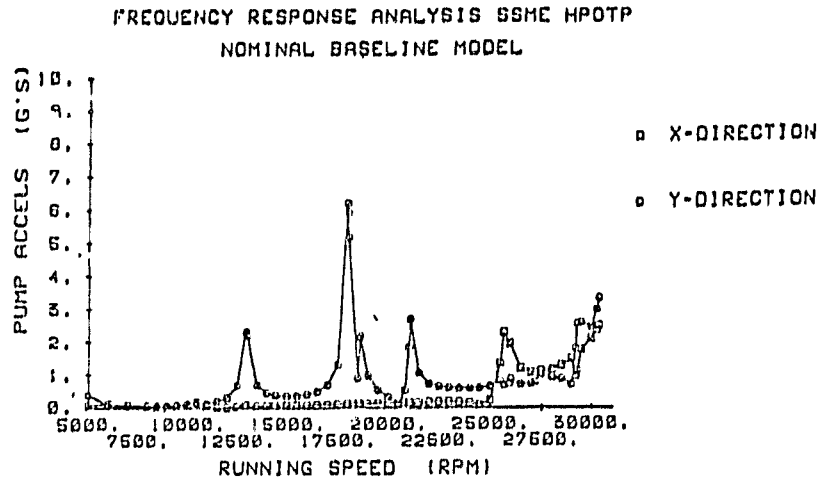


Figure 5(b). Pump accelerometer levels in the X-Z and Y-Z planes.

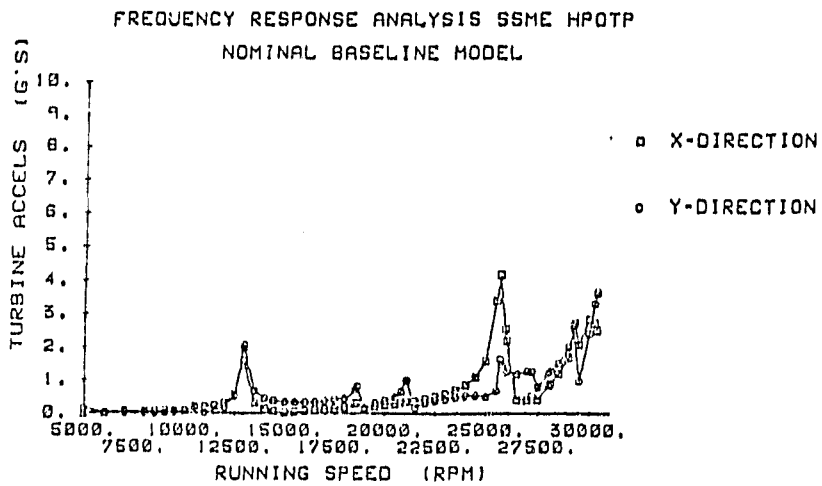


Figure 5(c). Turbine accelerometer levels in the X-Z and Y-Z planes.

are responsive to the "rotor" critical speeds, the housing accelerometer levels may respond more sharply to rotor-housing combined modes. This is particularly true for the first critical speed at approximately 12,500 cpm. However, the predicted accelerometer levels are quite responsive to motion associated with the "rotor" second critical speed at approximately 32,500 cpm.

The above results support the following conclusions with respect to the dynamic characteristics of the HPOTP:

(a) Response. The proximity of the second critical speed to FPL is a continuing cause for concern with respect to excessive bearing loads. Even modest losses of bearing stiffnesses are sufficient to drop the second critical speed into the operating range.

(b) Stability. Based on the prior "400 Hz" experience with this turbopump, the second critical speed appears to be lightly damped and subject to instability.

Changes in the turbine-interstage seal coefficients for the current (convergent-tapered) and prior (constant-clearance) configurations made no appreciable difference in the rotordynamic characteristics of the nominal model with respect to second-critical speed response.

## Seal Modifications with the Current Rotor

### *Boost Impeller Wear-Ring Seals*

Figure 6 illustrates the predicted bearing reactions which results with damper seal configurations for the boost impeller, and a comparison of this result with the nominal-rotor-model results of figure 5 (a) indicates a sharp reduction in peak bearing-reaction magnitudes. Additionally, the OSI is increased from 30,480 to 36,350 cpm.

### *Shrouded Inducer Seals*

Figure 7 illustrates the results for the shrouded inducer configuration. Stated

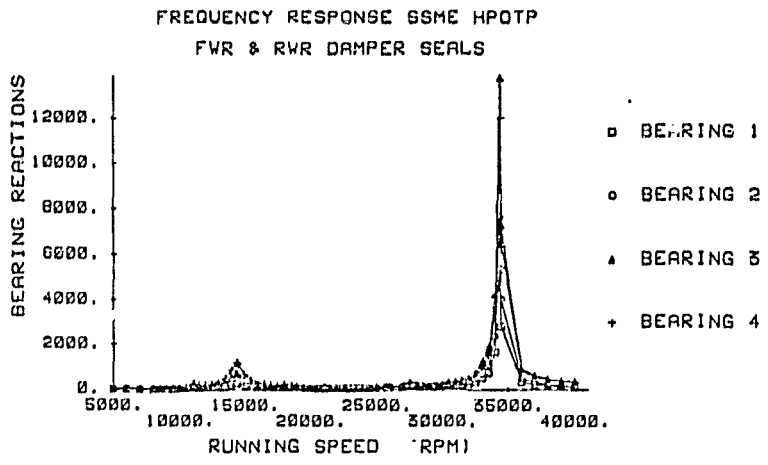


Figure 6. Bearing reactions for the nominal linear model with "damper" seal coefficients for boost-impeller seals.

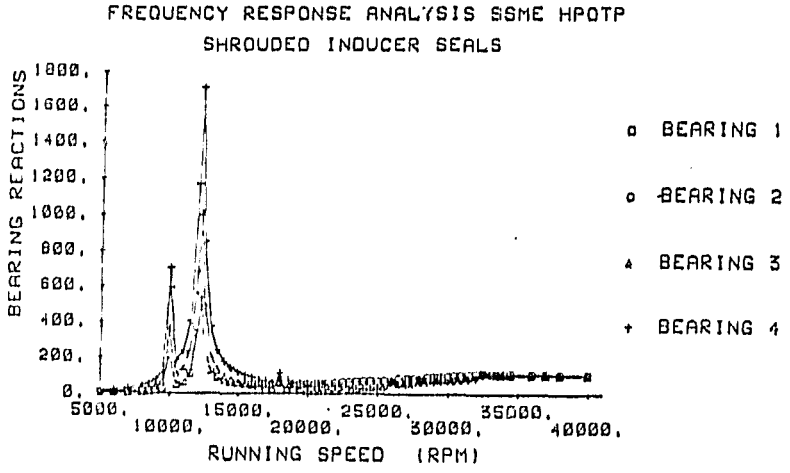


Figure 7. Bearing reactions for the nominal rotor model with "damper" seal coefficients for a shrouded inducer.

briefly, the second critical speed is simply eliminated for this configuration, and the OSI is increased to 59,950 cpm.

Stiffened Rotor Results

Figure 8 illustrates rotor-housing mode shapes which are dominated by the rotor motion and correspond to the first and second rotor critical speeds. Observe that the modeshapes are similar to those of figure 3 but that the natural frequency associated with the second critical speed has been increased from 530 Hz to 558 Hz. This increase is the expected result associated with an increase in rotor stiffness. However, the corresponding result for the overhung turbine mode is a decrease from 179 Hz to 168 Hz, which is certainly not expected. Bob Beatty at Rocketdyne feels that the results for the original rotor model are in error because of a low mass estimate in the turbine disks. Specifically, the mass due to goldplating was not accounted for in the original analysis.

*Stiffened-Rotor/Boost-Impeller-Labyrinth-Seal Model*

Figure 9 illustrates the bearing-reaction-magnitudes versus speed results when the nominal rotor structural-dynamic-model data is replaced with the stiff-rotor-model data. Observe that the second critical speed is elevated from approximately 32,500 cpm to 35,000 cpm, and that the FPL bearing loads are reduced. The OSI is increased to approximately 40,000 cpm.

*Stiffened-Rotor/Boost-Impeller Damper Seal*

Figure 10 illustrates the bearing-reaction-magnitude versus speed results for a stiffened-rotor/damper-seal configuration. By comparison to figure 9, the second critical speed is elevated to 42,000 cpm, and the peak bearing-reaction magnitudes are decreased. For this configuration, the OSI is increased to approximately 45,000 rpm.

*Stiffened Rotor/reduced-Stiffness Boost-Impeller Damper Seals*

The predicted direct stiffness of a damper-seal configuration for the boost-

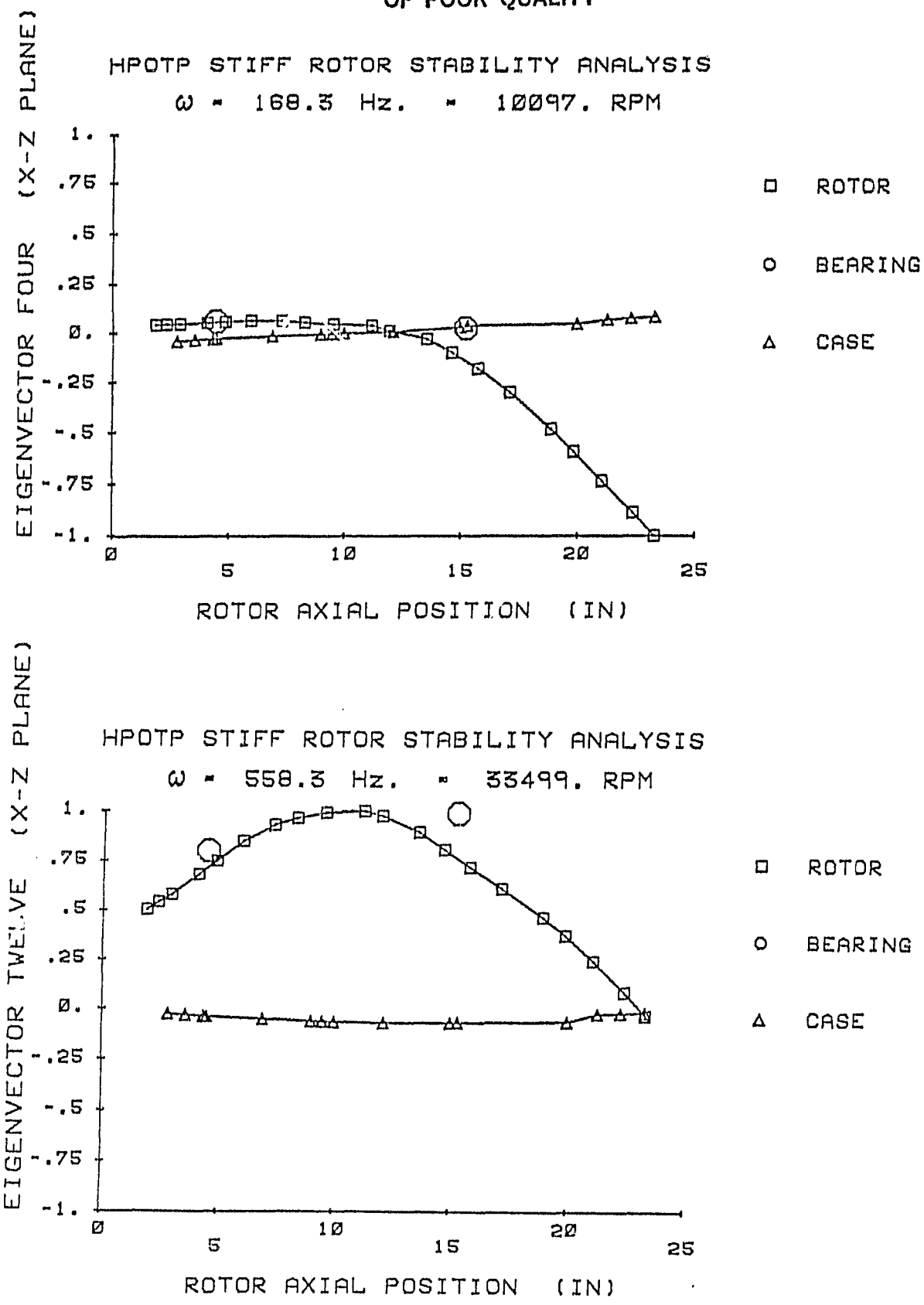


Figure 8. Undamped, zero-running-speed, stiffened-rotor/housing modes associated with the first and second critical speeds.

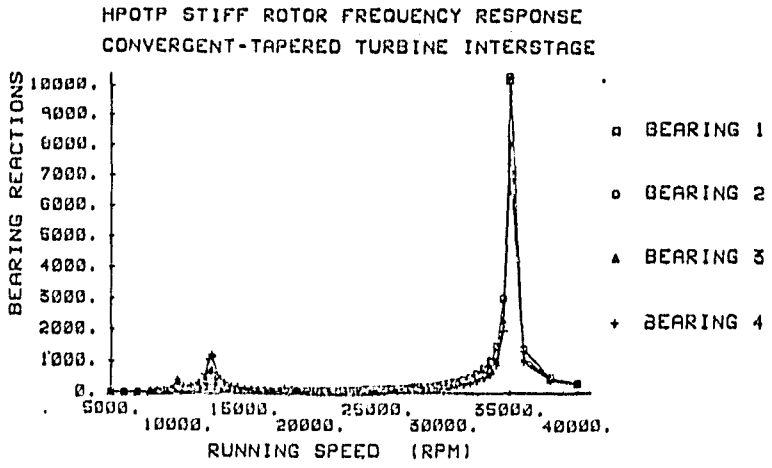


Figure 9. Bearing reaction magnitudes versus running speed for the stiffened-rotor model with labyrinth boost-impeller seals

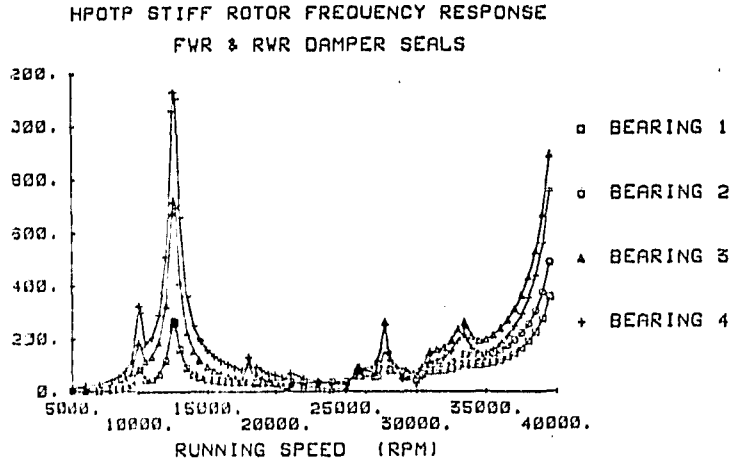


Figure 10. Bearing-reaction magnitudes versus running speed for the stiffened-rotor model with damper seals for the boost impeller.

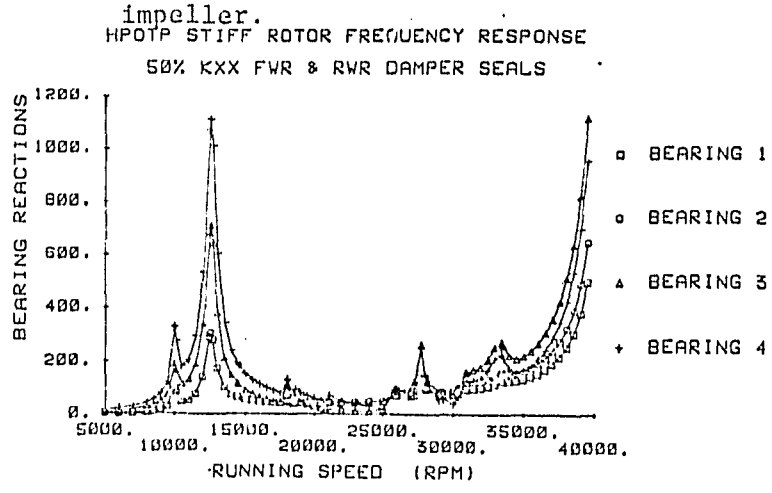


Figure 11. Bearing-reaction magnitudes versus running speed for the stiffened-rotor model with reduced-stiffness damper seals for the boost impeller.

impeller discharge seal is comparable to that of the bearings and acts to markedly reduce the amplitude of relative rotor motion at the seal location. Beyond a certain point, increasing the seal's direct stiffness becomes counterproductive in that the effectiveness of the seal's damping is limited in reducing synchronous-response amplitudes. Tests of seal stator configurations [15] suggest that seals can be developed with increased net damping and substantially decreased direct stiffness coefficients. The results of figure 11 illustrate the consequences of a 50% reduction in the predicted direct stiffness coefficient of the boost-impeller damper seals. While the bearing reaction magnitudes are relatively unchanged, the OSI for the arrangement is sharply elevated to 62,000 cpm.

## SUMMARY AND CONCLUSIONS

Table 3 contains a summary of the pertinent results for linear analysis. An assessment of the results presented in figures 6 through 11 and table 3 supports the following conclusions:

*Current Rotor*

(a) Modification of the boost impeller seals has the potential for significantly reducing bearing reactions at FPL; however, the second critical speed remains only slightly above FPL and any loss of bearing stiffness will drop it into the operating range.

(b) The damper-seal modification yields a predicted increase of the OSI by 19%.

(c) The shrouded-inducer design eliminates both the second critical speed and the stability problem.

| Configuration | 2nd Critical speed (cpm) | OSI (cpm) | Whirl Freq. (Hz) | FPL Bearing Reaction (lbs) | | | |
|---|---|---|---|---|---|---|---|
| | | | | 1 | 2 | 3 | 4 |
| Nominal | 32,500 | 30,480 | 536 | 553 | 635 | 667 | 548 |
| Nominal with Damper Boost-Impeller Seals | 34,000 | 36,350 | 576 | 251 | 349 | 513 | 411 |
| Nominal with Shrouded Inducer Seals | critically damped | 60,000 | 80 | 80 | 85 | 56 | 58 |
| Stiffened Rotor | 35,000 | 40,154 | 583 | 305 | 314 | 229 | 173 |
| Stiffened Rotor with Damper Seals | 42,000 | 45,000 | 701 | 64 | 82 | 90 | 54 |
| Stiffened Rotor with 50% stiffness Damper Seals | 62,000 | 44,000 | 700 | 82 | 99 | 102 | 66 |

Table 3. Linear OSI, whirl frequency, 2nd critical-speed location, and FPL bearing reactions.

*Stiffened Rotor*

(a) Stiffening the rotor, without changing the seals, yields a substantial elevation of both the OSI (32%) and the second critical speed (29%), and a sharp reduction in FPL bearing loads. Assuming that the structural dynamic models accurately reflect the relative stiffness of the two rotors, stiffening the rotor provides a marked improvement in the rotordynamic characteristics of the turbopump.

(b) Boost-impeller damper seals provide a significant additional improvement in the dynamic characteristics of the HPOTP, primarily in reduction of FPL bearing loads.

(c) Reducing the direct stiffness of the boost-impeller damper seals mainly acts to elevate the OSI with minimal increases in FPL bearing loads.

## NONLINEAR ANALYSIS PROCEDURES AND RESULTS

### Introduction

As noted previously, the bearing "dead-band" clearances provide the essential nonlinearity in the HPOTP model. The bearing clearances interact with the effects of side loads and rotor imbalance to yield significantly different results for a nonlinear model than those predicted by linear models.

Figure 12 illustrates the analytical model used by Yamamoto [3] to investigate the influence of bearing clearances on rotordynamic response in the absence of side loads. For zero bearing clearances, the model of figure 12 reduces to a simple Jeffcott model with viscous external damping. Figure 13 illustrates the response characteristics for a progressive increase in the ratio of bearing clearance to imbalance eccentricity $\hat{e} = e/a$. The results are for a damping ratio of 2.5%, and indicate that the speed location of maximum bearing reactions is reduced by increasing $\hat{e}$. Moreover, the drop in amplitude for speeds above the maximum bearing-load can be precipitious. The response characteristics of figure 13 can give rise to "jump" phenomena with the synchronous vibration level jumping either up or down for very small changes in running speed. Flight data for the HPOTP have demonstrated sudden step increases in accelerometer levels.

From these results, one would anticipate that bearing clearances could easily drop the peak-bearing-load running speed location associated with the second critical speed into the operating range. In fact, parametric studies of the bearing clearances clearly confirm this result [1]. They also confirm that peak-bearing-load speeds can be reduced below FPL for sufficiently large clearances. Hence for a given running speed, a nonlinear model with bearing

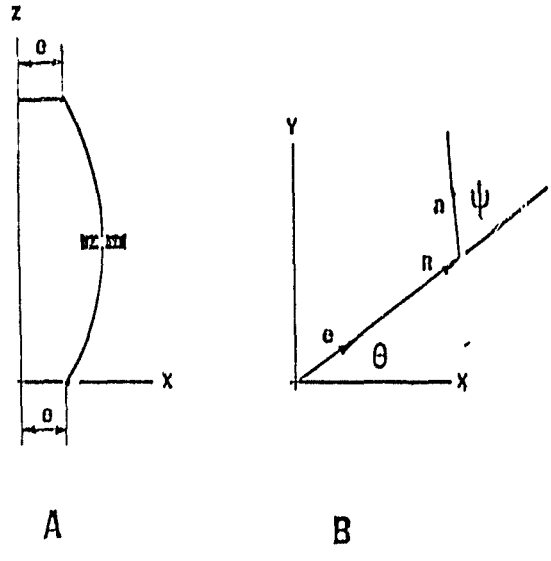


Figure 12. Yamamoto's model for synchronous response with bearing clearances.

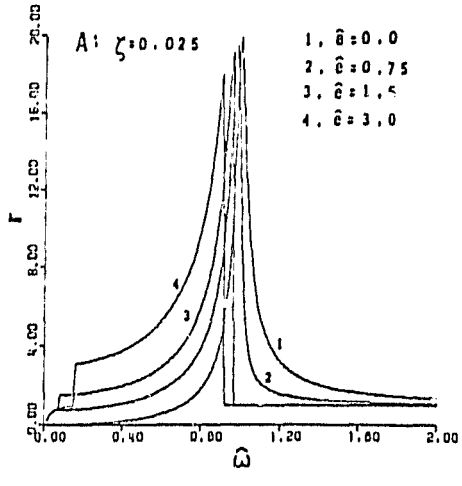


Figure 13. Synchronous-response characteristics for Yamamoto's model with increasing bearing clearances.

clearances can yield either substantially larger or smaller bearing reactions than the linear model.

The nonlinear simulation results of this section were developed for the following purposes:

(a) develop an explanation for the observed 450 Hz whirl frequency, and

(b) evaluate the effectiveness of proposed hardware remedies for improving the rotordynamic characteristics of the HPOTP.

Current Rotor Configuration

The nonlinear model was verified by comparison to results from the linear model, e.g., the second-critical-speed location at 32,500 cpm was obtained for zero bearing clearances. Figure 14 illustrates the bearing 2 reaction magnitude and turbine acceleration signals at FPL for the nominal model with the bearing clearances of Eq. (2). Observe the "clipping" of the bearing reaction magnitudes in figure 14 (a), which results from motion through the bearing dead-band. Motion in and out of the dead-band results as a combination of static displacement due to side loads and elliptical orbits due to imbalance. Bearing clipping generates a nearly periodic impulsive loading at the bearings that excites the beating motion which is evident in the accelerometer signal prediction of figure 14 (b). Spectrum analysis results of the accelerometer signals at FPL and two higher speeds are provided in figure 15 and reveal a subsynchronous signal at 26,500 cpm (443 Hz). Both the synchronous and subsynchronous signals are observed to decrease as the running speed increases. Observe that the frequency of the subsynchronous motion is consistent with frequencies observed in test data as apposed to the linear predictions of 530 Hz. The linear model corresponding to the result of figure 14 is lightly damped but stable. The nonlinear

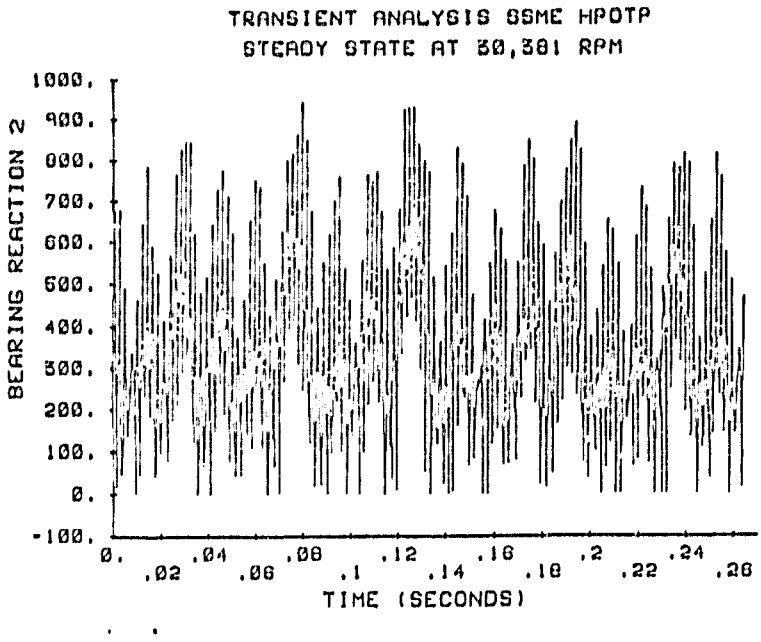


Figure 14(a). Bearing 2 reaction magnitude versus time at FPL for the nominal nonlinear model.

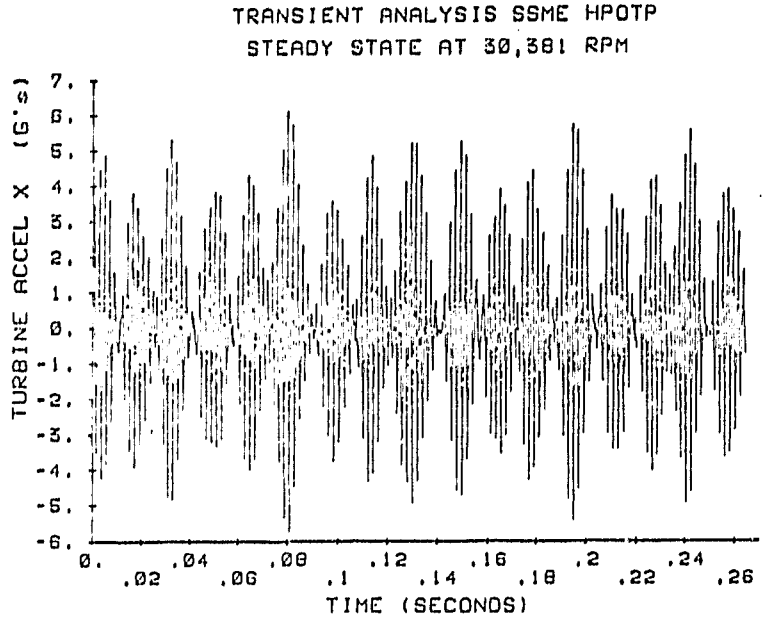


Figure 14(b). Turbine X-Z plane acceleration magnitude versus time for the nonminal nonlinear model.

model remains in a limit cycle motion with subsynchronous components until the clearance-excitation-force coefficients at the main impeller are increased to 250% of their nominal values, but then diverge exponentially. Based on these observations, the subsynchronous component of figure 14 is deemed to be the result of bearing nonlinearities and not the result of an instability. However, the nonlinear subharmonic motion can only be developed for light rotor damping, and the rotor is certainly unstable for zero bearing stiffnesses which is the case when motion is within the dead-bands.

The subsynchronous motion of figures 14 and 15 arises at speeds above the maximum synchronous response speed predicted by Yamamoto's model in figure 13. This statement is supported by the results in figure 16 which shows the bearing 2 reaction magnitude predictions at 29,450 cpm. Observe that the synchronous bearing-reaction magnitudes are significantly higher than the subsynchronous amplitudes of figure 14 (a).

A second nonlinear model configuration which yielded a substantial subsynchronous vibration component was obtained by doubling both the imbalance magnitudes and the destabilizing force coefficients at the main impeller, adding damping at the bearing (2 lb s/in), and increasing the damping at the main impeller to 15 lb s/in. This configuration is predicted to be linearly stable at FPL. Spectral analysis results for this configuration at FPL and two higher speeds are presented in figure 17. In this case, the subsynchronous component increases with running speed, while the synchronous component decreases.

Figures 18 through 20 illustrate results for the nominal nonlinear rotor model with damper seals at the boost impeller. By comparison to figure 16, observe that the damper seals significantly reduces the RPL synchronous loads and the constant side loads on bearing 2. By comparison to figure 14 (b), figure 19

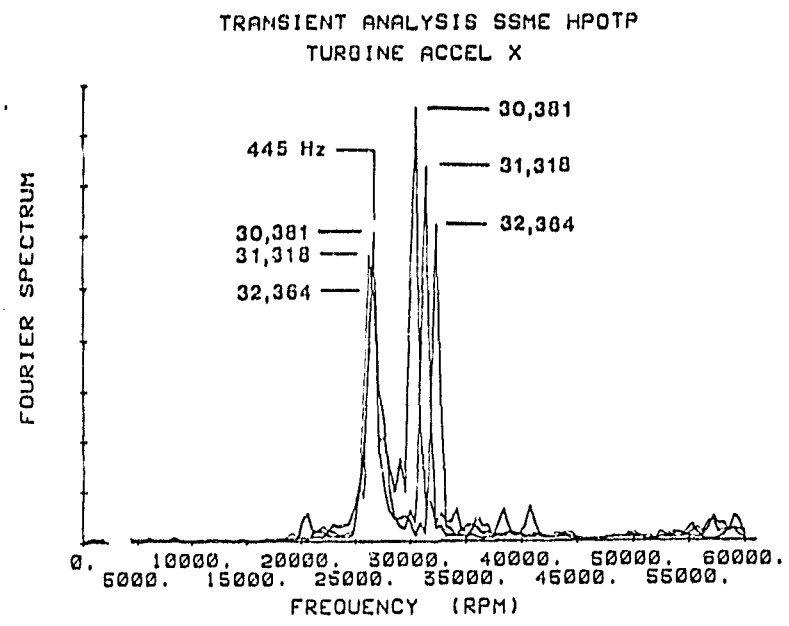


Figure 15. Turbine X-Z plane acceleration spectr at FPL and higher speeds for the nominal nonlinear model.

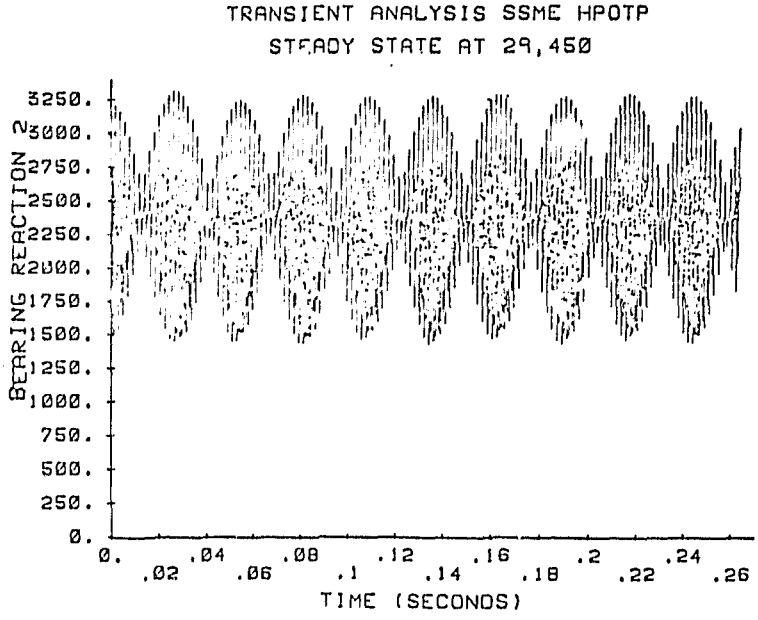


Figure 16. Bearing 2 reaction magnitude at 29,500 cpm for the nominal nonlinear model.

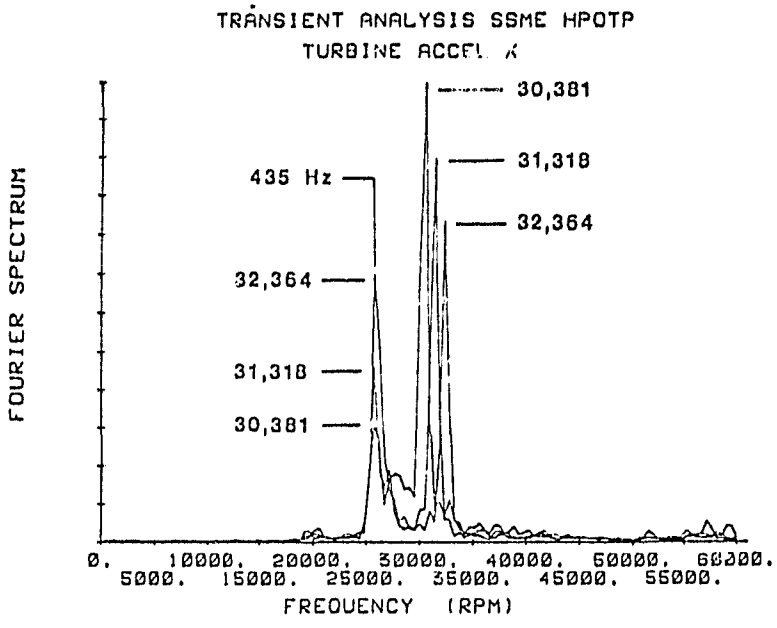


Figure 17. Turbine X-Z plane acceleration spectra at FPL and higher speeds for nonlinear model number 2.

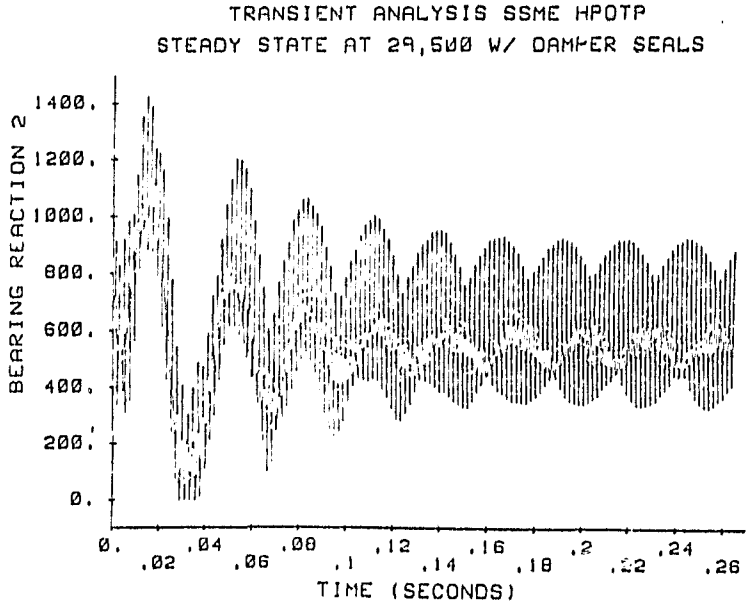


Figure 18. Bearing 2 reaction magnitude at 29,500 cpm for the nominal nonlinear model with damper seals at the boost impeller.

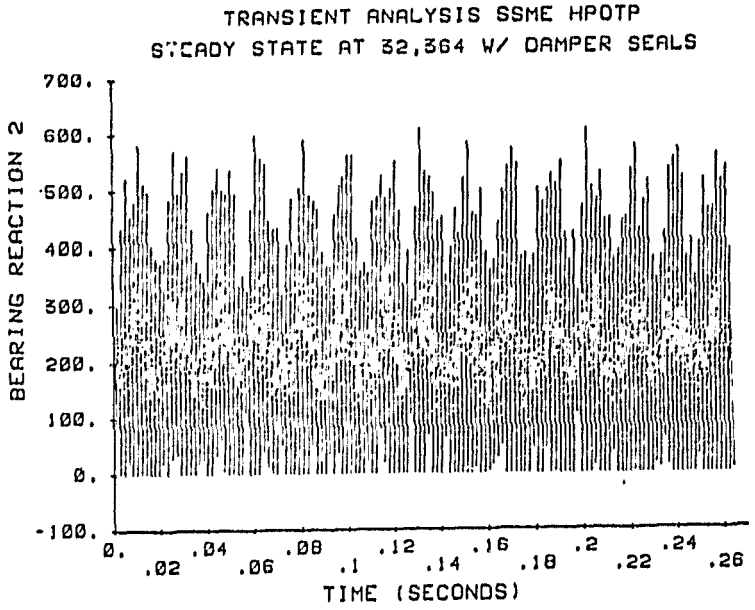


Figure 19. Bearing 2 reaction magnitude at speeds above FPL for the nominal nonlinear model with damper seals at the boost impeller.

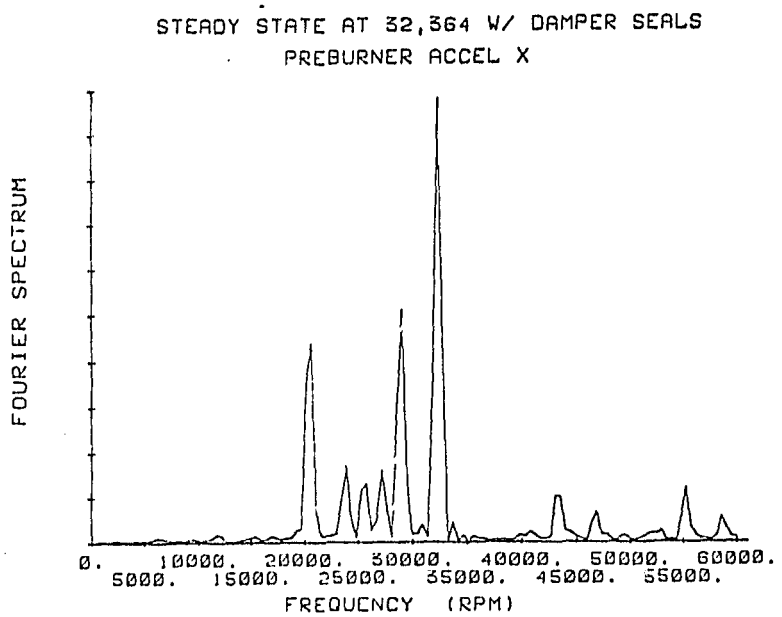


Figure 20. Preburner X-Z accelerometer spectrum at FPL for the nominal nonlinear model with damper seals at the boost impeller.

demonstrates that the damper seals significantly alter the nature of the subsynchronous motion, but tend to increase the "clipping" of the bearing reactions. Presumably, the clipping motion is increased because of the direct stiffness of the damper seals which tends to counter the side loads and center the bearings within their clearances. The spectra of figure 20 demonstrate that the subsynchronous motion remains significant for the nominal rotor model with boost-impeller damper seals.

Stiffened-Rotor Results

The results of the preceding section examine the consequences of a change in the current boost-impeller wear-ring seals from a labyrinth to a damper-seal design with no stiffening of the rotor. Conversely, the frames of figure 21 illustrate the consequences of introducing the stiffened rotor without changing the seals. Observe that the FPL bearing reactions and acceleration levels have actually increased as compared to the nominal model of figure 14 which contradicts the linear predictions. Introducing the stiffened rotor elevates the second critical speed and eliminates motion in and out of the bearing dead-bands. Presumably, at some higher running speed, the dead-band motion and associated subsynchronous motion would return. Fourier analysis of the acceleration signal of figure 21 (b) shows synchronous and twice synchronous components but no subsynchronous.

At present, the stiffened-rotor and boost-impeller damper seals are a "package-deal" in that all modified units will incorporate both changes. Figure 2 illustrates predicted FPL results for this configuration. Observe by comparison to figures 14 and 21 that the bearing -2 reaction magnitude and the turbine -X accelerations are both reduced substantially. Fourier spectrum analysis of the accel. signal of figure 22 (b) reveals synchronous and twice-synchronous components, but no subsynchronous.

Concerning the vibration characteristics at RPL, the results of figure 23 illustrate a sharp reduction in the bearing -2 reaction magnitude as compared to figure 16. Fourier analysis of the turbine acceleration signal of figure 23 (b) reveals no subsynchronous components.

One precautionary note is emphasized with respect to the encouraging bearing-reaction predictions of figures 22 (a) and 23 (a). The model is set up so that the boost-impeller seals and bearings are exactly centered. Hence, the seals act to unload the bearing alternating and constant loads. However, if the centers are radially displaced the seal stiffness would act to increase the steady-state bearing reaction magnitude.

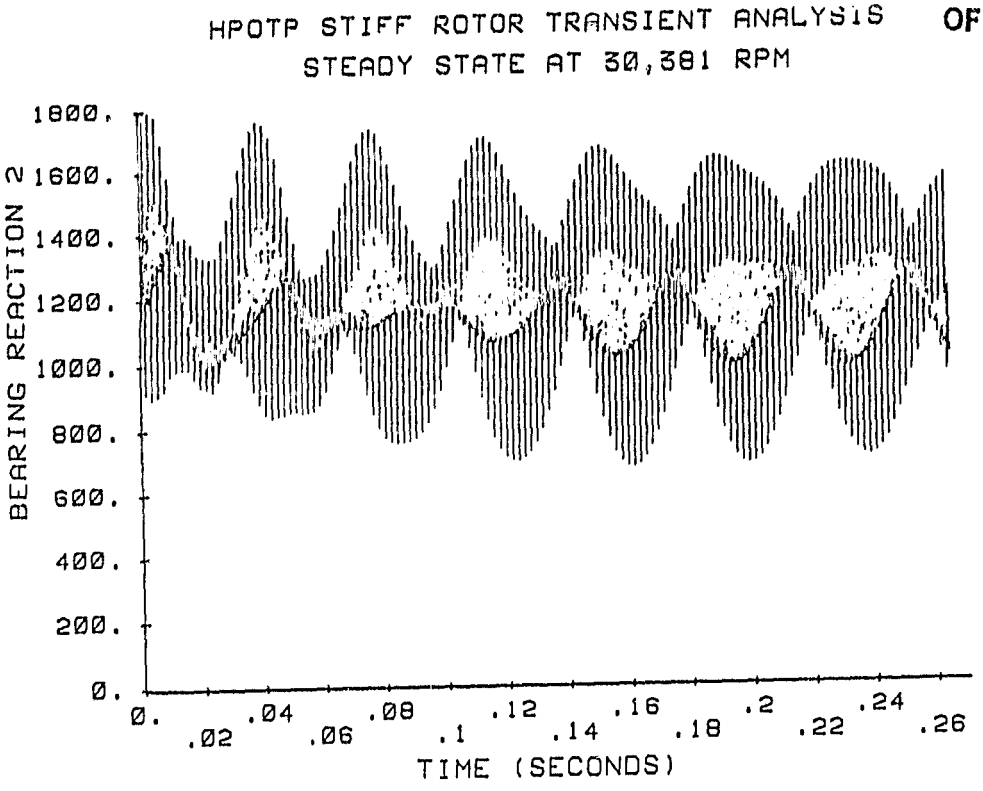


Figure 21 (a). Bearing 2 reaction magnitude versus time at FPL for the stiffened rotor with labyrinth, boost-impeller, wear-ring seals.

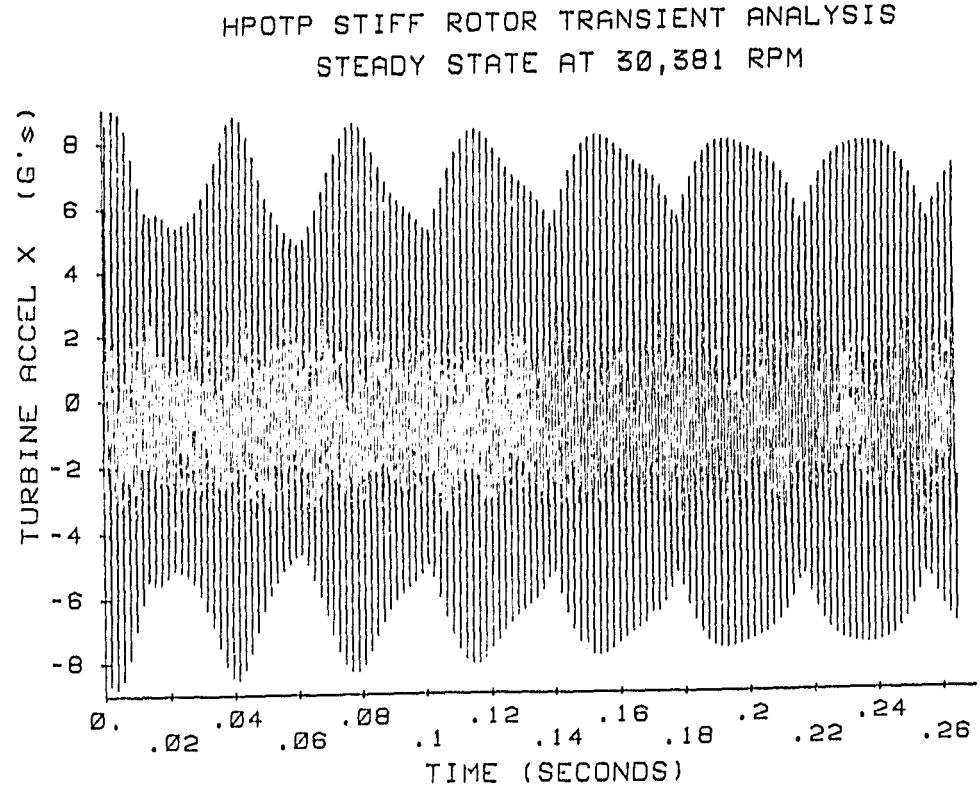


Figure 21 (b). Turbine acceleration level versus time at FPL for the stiffened-rotor with labyrinth, boost-impeller wear-ring seals.

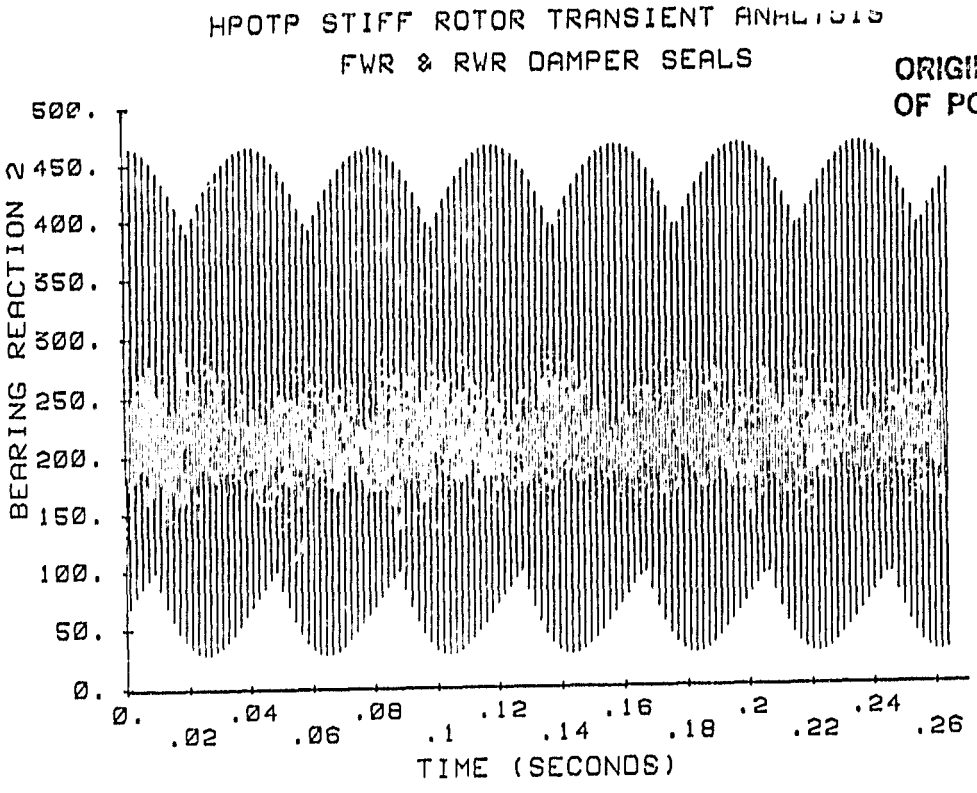


Figure 22 (a). Bearing 2 reaction magnitude versus time at FPL for the stiffened rotor with damper-seal designs for the boost-impeller wear-ring seals.

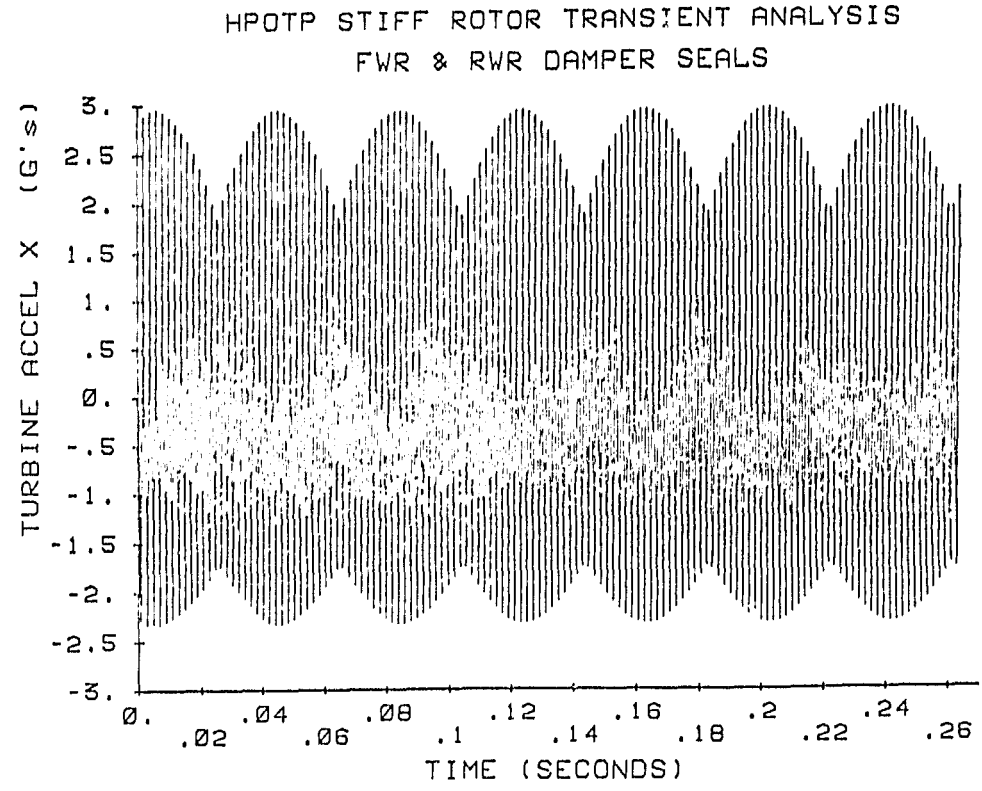


Figure 22 (b). Turbine acceleration level versus time at FPL for the stiffened rotor with damper-seal designs for the boost-impeller, wear-ring seals.

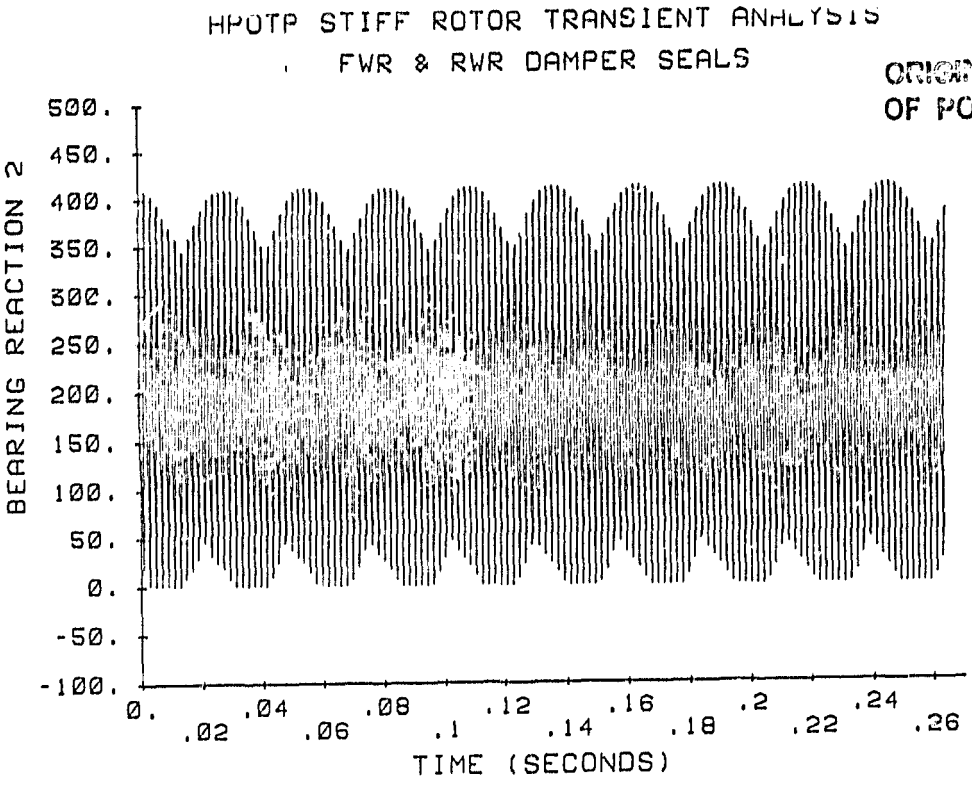


Figure 23 (a). Bearing 2 reaction magnitude versus time at FPL for the stiffened-rotor/boost-impeller damper seal configuration.

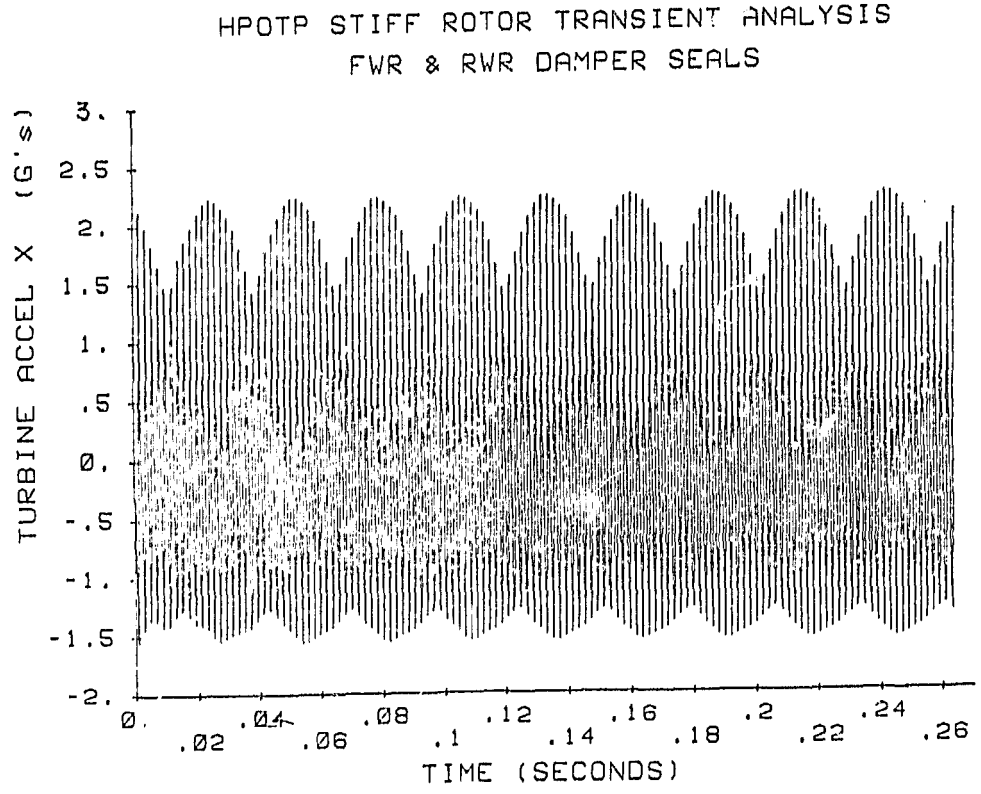


Figure 23 (b). Turbine X acceleration level versus time at FPL for the stiffened rotor/boost-impeller damper seal confuguration.

## CONCLUSIONS

Linear and nonlinear analyses of the HPOTP support the following conclusions:

(a) By linear predictions, the second critical speed of the current (unstiffened-rotor) HPOTP is only slightly above the FPL running speed and is lightly damped. Even a modest loss of bearing stiffness is sufficient to drop the second critical speed into the operating range and yield a prediction of excessive bearing loads.

(b) Based on prior test experience, the HPOTP appears to be lightly damped.

(c) The subsynchronous motion which is evident in test results can be obtained in a nonlinear model due to bearing clearances. Motion in and out of the dead-band clearances excites subharmonic motion for a stable but lightly damped model.

(d) A whirl frequency of subsynchronous motion at 440 Hz is predicted by the nonlinear model for the current rotor which is consistent with test results but at odds with a linear prediction of 530 Hz. This whirl frequency reduction results solely from the bearing clearances, and does not require any stiffness reduction in the model at the bearings or elsewhere.

(e) Bearing clearances can drop the peak-vibration running speed into the operating range yielding a prediction of excessive bearing loads at RPL.

(f) Incorporation of damper seals into the boost impeller seals with the current rotor markedly reduces predicted synchronous bearing

loads, but increases bearing-reaction clipping and subsynchronous motion at FPL.

(g) Introducing a stiffened rotor without changing the boost-impeller seals elevates the rotor critical speed and eliminates subsynchronous motion at FPL; however, predicted bearing-reaction magnitudes at FPL remain high.

(h) A stiffened-rotor/boost-impeller wear-ring damper seal configuration eliminates subsynchronous motion in the operating range and markedly reduces synchronous bearing reactions.

ACKNOWLEDGEMENTS

Discussions with Robert Beatty concerning a parallel investigation at Rocketdyne were very helpful in developing this report.

## APPENDIX A: INPUT DATA

### Current Rotor: Eigenvalues and Damping Factors

The rotor eigenvalues and eigenvectors used here are based on a model by B. Rowan. The free-free eigenvalues used are listed below.

$\lambda_1 = 0$ $\lambda_7 = 3724$ Hz

$\lambda_2 = 0$ $\lambda_8 = 4389$ Hz

$\lambda_3 = 426$ Hz $\lambda_9 = 6600$ Hz

$\lambda_4 = 970$ Hz $\lambda_{10} = 7397$ Hz

$\lambda_5 = 1561$ Hz $\lambda_{11} = 10396$ Hz

$\lambda_6 = 2698$ Hz $\lambda_{12} = 11916$ Hz

One-half percent of critical damping was used for modes three through twelve. Zero damping was used for modes 1 and 2.

### Stiffened Rotor: Eigenvalues and Damping Factors

The rotor eigenvalues and eigenvectors used here are based on a 1983 model provided by Robert Beatty of Rocketdyne.

$\lambda_1 = 0$ $\lambda_7 = 3211$ Hz

$\lambda_2 = 0$ $\lambda_8 = 3787$ Hz

$\lambda_3 = 451$ Hz $\lambda_9 = 4722$ Hz

$\lambda_4 = 1053$ Hz $\lambda_{10} = 5571$ Hz

$\lambda_5 = 1779$ Hz $\lambda_{11} = 6879$ Hz

$\lambda_6 = 2998$ Hz $\lambda_{12} = 7604$ Hz

One-half percent of critical damping was used for modes three through twelve. Zero damping was used for modes 1 and 2.

### Housing Eigenvalues and Damping Factors

The case eigenvalues and eigenvectors are based on a 1982 Rocketdyne structural-dynamic model. The eigenvalues used in the study are

| | |
|---|---|
| $\lambda_{c1}$ = 45 Hz | $\lambda_{c6}$ = 351 Hz |
| $\lambda_{c2}$ = 86 Hz | $\lambda_{c7}$ = 432 Hz |
| $\lambda_{c3}$ = 111 Hz | $\lambda_{c8}$ = 468 Hz |
| $\lambda_{c4}$ = 300 Hz | $\lambda_{c9}$ = 488 Hz |
| $\lambda_{c5}$ = 310 Hz | $\lambda_{c10}$ = 542 Hz |

One-half percent of critical damping was used for all housing modes.

Seal Rotordynamic Coefficients

Experience has shown that turbopump seals have a very significant influence on rotordynamics. Because of the HPOTP modeshapes, the turbine seals have a predominant influence on the first-critical response and minimal influence on the second-critical response. Conversely, seals at the boost or main impeller have a significant influence on motion associated with the second critical speed, but minimal influence on motion associated with the first critical speed. To improve rotordynamic response, the following seal changes have been implemented or considered:

(a) The turbine interstage seal was first changed from a stepped labyrinth to a constant-clearance/honeycomb-stator configuration, and then to a convergent-taper/honeycomb-stator configuration.

(b) The boost-impeller wear-ring seals have been changed (in test pumps) from labyrinth to constant-clearance seals with roughened stators.

(c) Sealing surfaces are to be created at the outer surface of shrouded inducers for the main impeller.

Rocketdyne-calculated rotordynamic coefficient values (1977) are used for labyrinth seals, viz., the turbine tip seals and boost-impeller labyrinth seals. Rocketdyne-calculated values are also used for the shrouded-inducer

seals. However, TAMU calculated values are used for the boost-impeller damper seals, the high-pressure-turbine, and the turbine interstage seals. The analysis of Childs and Kim [12] is used for incompressible-fluid seals and the analysis of Nelson [16] is used for gas seals. For completeness, input data for these calculations are also provided.

Tables A.1 and A.2 contain the appropriate data for the boost-impeller seals, while tables A.3 and A.4 contain data for the high-pressure turbine seal and the turbine interstage seal. Data for the remaining seals are provided in table A.5 and A.6.

| Seal | Power Level | D (in) | L (in) | $C_r$ (in) | $u^*_{\theta o}$ --- | $\gamma$ lb/ft$^3$ | $\mu \times 10^6$ lb sec/ft$^2$ | $\Delta P$ psi | $\dot{w}$ cpm |
|---|---|---|---|---|---|---|---|---|---|
| Inlet | FPL | 2.89 | 0.5 | .006 | .25 | 70.2 | .373 | 2006 | 30,367 |
| | MPL | 2.89 | 0.5 | .007 | .25 | 70.6 | .385 | 970 | 20,298 |
| Discharge | FPL | 3.345 | 0.87 | .004 | 1.0 | 70.2 | .373 | 6505 | 30,367 |
| | MPL | 3.345 | 0.87 | .0048 | 1.0 | 70.6 | .373 | 3246 | 20,298 |

$^*u_{\theta o} = U_{\theta o}/(R\omega/2)$ = Normalized inlet tangential velocity

Turbulence Empirical Coefficients

Stator: ms = -0.136, ns = -.1357

Rotor: mr = -0.25, nr = .079

Table A.1 Input data for boost-impeller damper seal calculations.

| Seal | Power Level | K lb/in | k lb/in | C lb sec/in | c lb sec/in | M X $10^4$ lb sec$^2$/in | m X $10^5$ lb sec$^2$/in | $\dot{w}$ lb/sec |
|---|---|---|---|---|---|---|---|---|
| Inlet | FPL | 112,340 (224,680) | 21,280 | 30. | 1.28 | 8.2 | - 1.44 | 8.37 |
| | MPL | 46,960 (93,920) | 8,800 | 18. | 0.72 | 6.86 | - 2.16 | 7.07 |
| Discharge | FPL | 732,220 (1.464 X $10^6$) | 369,800 | 280. | 14.8 | 80.6 | 20.00 | 8.28 |
| | MPL | 332,100 (664,000) | 151,690 | 163. | 8.42 | 67.3 | 17.0 | 7.57 |

Table A.2 Calculated rotordynamic coefficients and leakage for boost-impeller seals.

Direct stiffness values in parenthesis were used in rotordynamic calculations and are twice calculated values.

| | Turbine I. S. | | H. P. Turbine | |
|---|---|---|---|---|
| | MPL | FPL | MPL | FPL |
| $\omega$ (cpm) | 20,283 | 30,376 | 20,283 | 30,376 |
| $P_{in}$ (psia) | 2,857 | 5,540 | 1,983 | 3,499 |
| $T_{in}$ (°R) | 1,024 | 1,498 | 897 | 111.9 |
| $P_{ex}$ (psia) | 2,354 | 4,261 | 45.6 | 63,4 |
| $R_g$ Ideal gas constant | 532 | 445 | 593 | 530 |
| $\mu$ (lbm/ft-sec) | $1.02 \times 10^{-5}$ | $1.44 \times 10^{-5}$ | $.92 \times 10^{-5}$ | $1.11 \times 10^{-5}$ |
| $\nu$ spec. heat ratio | 1.385 | 1.371 | 1.4 | 1.4 |
| R (in) | 2.867 | 2.867 | 1.316 | 1.316 |
| L (in) | 0.995 | 0.995 | 0.318 | 0.318 |
| $U_{\theta o}(o)/R\omega$ | 0.25 | 0.25 | 0.5 | 0.5 |

Turbine I. S. Seal

Constant (radial) clearance: $C_{in} = C_{ex} = .013$ in
Convergent taper: $C_{in} = 0.15$ in, $C_{ex} = .010$ in
Hirs' coefficient rotor: $m_r = -0.1634$, $n_r = .03757$
Hirs' coefficient stator: $m_s = -.002512$, $n_s = .01534$

H. P. Turbine Seal

Radial Clearance MPL: $C_{in} = .005$, $C_{ex} = .0016$
Radial Clearance FPL: $C_{in} = .0048$, $C_{ex} = .0013$
Hirs' coefficient rotor: $m_r = -.170$, $n_r = 0.040$
Hirs' coefficient stator: $m_s = -0.143$, $n_s = 0.030$

Table A.3 Input data for turbine gas seals.

| Seal | Power Level | K X $10^{-5}$ lb/in | k lb/in | C lb/in | c lb/in | $\dot{w}$ lb/sec |
|---|---|---|---|---|---|---|
| Turbine H.P. | FPL | 1.965 | 4,140 | 2.51 | .015 | .0335 |
| | MPL | 1.016 | 1,560 | 1.39 | .005 | .0238 |
| Turbine I.S. Const. Clearance | FPL | 2.02 | 9,440 | 11.3 | .067 | .7427 |
| | MPL | .918 | 3,050 | 6.56 | .041 | .3000 |
| Turbine I.S. Convergent Taper | FPL | 1.05 | 10,000 | 10.0 | .042 | .6263 |
| | MPL | .420 | 3,880 | 4.80 | .027 | .2557 |

Table A.4 Rotordynamic coefficients and leakage for the high-pressure turbine seal and the turbine interstage seal.

| | K | k | C | c |
|---|---|---|---|---|
| | lb/in | lb/in | lb sec/in | lb sec/in |
| Boost-Impeller Inlet (labyrinth) | 1206. | 740. | .712 | $4.43 \times 10^{-3}$ |
| Boost-Impeller Discharge (labyrinth) | 10,000. | 5,470. | 5.26 | $63.3 \times 10^{-3}$ |
| Second-stage Turbine Tip Seal | 6,207. | 777. | .738 | $22.3 \times 10^{-3}$ |
| First-stage Turbine Tip Seal | 5,739. | 568. | .547 | $20.3 \times 10^{-3}$ |
| Shrouded Inducer (one seal) | 62,000 | 65,000 | 98. | 0.0 |

A.5 Rocketdyne-calculated rotordynamic coefficients for labyrinth seals and shrouded-inducer selas at MPL; $\omega$ = 20,218 cpm

| | K | k | C | c |
|---|---|---|---|---|
| | lb/in | lb/in | lb sec/in | lb sec/in |
| Boost-Impeller Inlet (labyrinth) | 2610. | 1760. | 1.08 | $5.79 \times 10^{-3}$ |
| Boost-Impeller Discharge (labyrinth) | 27,690. | 15,133. | 9.33 | $131. \times 10^{-3}$ |
| Second-stage Turbine Tip Seal | 6,207. | 4,560. | 2.93 | $89.7 \times 10^{-3}$ |
| First-stage Turbine Tip Seal | 5,739. | 4,640. | 32.86 | $92.9 \times 10^{-3}$ |
| Shrouded Inducer (one seal) | 154,000 | 165,000 | 166.0 | 0.0 |

A.6 Rocketdyne-calculated rotordynamic coefficients for labyrinth seals and shrouded-inducer seals at FPL; $\omega$ = 30,381 cpm.

REFERENCES


1. D. W. Childs, "Rotordynamics Analysis for the HPOTP (High Pressure Oxygen Turbopump) of the SSME (Space Shuttle Main Engine), "an Interim Progress Report for NASA Contract NAS8-31233, Speed Scientific School, the University of Louisville, Louisville, Ky., 15 September 1979.

2. T. Yamamoto, "On Critical Speeds of a Shaft Supported by a Ball Bearing," ASME Trans. J. of Applied Mechanics, pp. 199-204, June 1959.

3. T. Yamamoto, "On the Critical Speeds of a Shaft," Memoirs of the Faculty of Engineering, Nagogo University, Vol. 6, No., 2, 1954.

4. D. W. Childs, "Definition of Forces on Turbomachinery Rotors - Task A Report," Turbomachinery Laboratories, Mechanical Engineering Department, Texas A&M University, February 1983.

5. D. W. Childs, "Definition of Forces on Turbomachinery Rotors - Task B Report: Dynamic Analysis of Rotors, "NASA MSFC Contract NAS8-34505, Turbomachinery Laboratories Report, RD-2-83, 1 May 1983.

6. R. F. Beatty and B. F. Rowan, "Determination of Ball Bearing Dynamic Stiffness," Proceedings, Second Workshop on Rotordynamic Instability Problems in High Performance Turbomachinery, NASA CP 2250.

7. A. B. Jones, "A General Theory for Elastically Constrained Ball and Radial Roller Bearings Under Arbitrary Load and Speed Conditions," ASME J. of Basic Engineering, Vol. 82, No. 2, pp. 309-320, June 1960.

8. H. F. Black and E. A. Cochrane, "Leakage and Hybrid Bearing Properties of Serrated Seals in Centrifugal Pumps," Paper G5, 6th International Conference in Fluid Sealing, Munich, German Federal Republic, 27 February - 2 March 1973.

9. H. F. Black and D. N. Jensen, "Effects of High-Pressure Ring Seals on Pump Rotor Vibrations," ASME Paper No. 71-WA/FE-38, Winter Annual Meeting, Washington, D. C., 1971.

10. H. F. Black, P. E. Allaire, and L. E. Barrett, "The Effect of Inlet Flow Swirl on the Dynamic Coefficients of High-Pressure Annular Clearance Seals," Ninth International Conference on Fluid Sealing, BHRA Fluid Sealing Conference, Leeuwenhorst, The Netherlands, April 1981.

11. G. L. von Pragenau, "Damping Seals for Turbomachinery," NASA TP-1987, March 1982.

12. D. W. Childs and C-H. Kim, "Analysis and Testing for Rotordynamic Coefficients of Turbulent Annular Seals with Different, but Directionally-Homogeneous Surface-Roughness Treatments for Rotor and Stator Elements," to be submitted for 1984 ASME-ASLE Conference and ASME J. of Tribology.

13. D. W. Childs, "Finite-Length Solutions for Rotordynamic Coefficients of Turbulent Annular Seals," ASME Trans. J. of Lubrication Technology, Vol. 105, pp. 437-445, July 1983.

14. H. Benchert and J. Wachter, "Flow Induced Spring Coefficients of Labyrinth Seals for Applications in Rotordynamics," NASA CP 2133, Proceedings of the Workshop on Rotordynamic Instability Problems in High-Performance Turbomachinery, pp. 189-212, 12-18 May 1980.

15. D. W. Childs, SSME Interstage Seal Research Progress Report - Contract NAS8-33716," for NASA MSFC. Turbomachinery Laboratories, Mechanical Engineering Department, Texas A&M University, Report No. SEAL-1-84, January 1984.

16. C. D. Nelson, "The Rotordynamic Coefficients of High-Pressure Annular Gas Seals," accepted for presentation at the 1984 ASME Gas Turbine Conference.

17. J. J. Thomas, "Instabilie Eigenschwingungen von Turbine Laufern, angefacht durch die Spaltstromungen Stopfbuchsen un Beschaufelungen, AEG-Sonderdruch, 1958.

18. J. Alford, "Protecting Turbomachinery From Self-Excited Rotor Whirl," ASME Trans. J. of Engineering for Power, 1958.

19. E. Hauck, "Measurement and Evaluation of Swirl-Type Flow in Labyrinth Seals," NASA CP 2250 Rotordynamic Instability Problems in High-Performance Turbomachinery, Proceedings of a workshop held at Texas A&M University, 10-12 May 1982.

20. D. S. Chamieh, A. J. Acosta, C. E. Brennen, T. K. Caughey, and R. Franz, "Experimental Measurement of Hydrodynamic Stiffness Matrices for a Centrifugal Pump Impeller," NASA CP 2250 Rotordynamic Instability Problems in High Performance Turbomachinery, Proceedings of workshop held at Texas A&M University, 10-12 May 1982.

21. A. J. Acosta, C. S. Brennen, T. K. Caughey, and B. Iberg," Measurement of Impeller - Inducer Rotor Forces for Evaluation of Dynamic Coefficients," presented at the ASME Applied Mechanics, Bioengineering and Fluids Engineering Conference, Houston, Texas, 20-22 June 1983.

22. S. Winder, "Data Input HPOTP Computer Simulation Model," ED14-05-78, NASA MSFC, 17 February 1978.

23. D. W. Childs, "The Space Shuttle Main Engine High-Pressure Fuel Turbopump Rotordynamic Instability Problem," ASME Trans. J. of Engineering for Power, Vol. 100, pp. 48-51, January, 1978.